

**FRACTURE STIMULATION IN
ENHANCED GEOTHERMAL
SYSTEMS**

**A REPORT SUBMITTED TO THE DEPARTMENT OF ENERGY
RESOURCES ENGINEERING**

OF STANFORD UNIVERSITY

**IN PARTIAL FULFILLMENT OF THE REQUIREMENTS FOR THE
DEGREE OF MASTER OF SCIENCE**

**By
Mark W. McClure
August 2009**

I certify that I have read this report and that in my opinion it is fully adequate, in scope and in quality, as partial fulfillment of the degree of Master of Science in Petroleum Engineering.

Prof. Roland N. Horne

(Principal Advisor)

Abstract

Enhanced Geothermal Systems (EGS) are geothermal reservoirs formed by hydraulic stimulation of low permeability rock. In faulted crystalline formations, the mechanism of stimulation is induced shear on preexisting fractures, which increases their transmissibility by orders of magnitude.

The processes that create fractured rock are discussed from the perspective of geology and rock mechanics. The European EGS project at Soultz-sous-Forêts, France is used as a case study of an EGS project. The focus is developing a solid conceptual understanding of the mechanism of hydraulic stimulation.

The second half of the report is concerned with stimulation modeling. Computer modeling offers tremendous power to describe the process of stimulation. It is argued that discrete fracture modeling, as opposed to an effective continuum, is the best approach for modeling EGS stimulation. This report lays out in detail how to construct a discrete fracture EGS stimulation model. Topics include geometry of the preexisting fractures, mass and energy transport, elastostatics (including the Displacement Discontinuity method), Coulomb frictional failure, and thermoelasticity. Finite difference, boundary element, and analytical approximations are applied where appropriate.

Applications of EGS stimulation modeling are numerous. They include (1) investigation of novel strategies for stimulation design, (2) optimization of wellbore orientation and spacing, (3) prediction of thermal breakthrough, (4) sensitivity study on the effect of different parameters, (5) prediction of intensity and location of microseismic events, (6) identification of geological settings that are advantageous for EGS.

Acknowledgments

First I would like to thank my advisor Professor Roland Horne. Whether he was advising me on academics when I was an undergrad (years before he was formally my advisor), driving classes on long field trips, discussing research, responding to emails at night and over the weekend, or attending our department's Friday afternoon socials, Roland has always been there for me. I have the deepest gratitude.

Thank you to my colleagues Zhe Wang and Egill Juliusson for our fruitful collaborations and stimulating discussions.

Thank you especially to Professor David Pollard, who met with me many times to share his expertise on fracturing, reviewed the manuscript of this thesis, and made many valuable comments. Also to Dr. Mohammad Karimi-Fard, who was very kind to share some of his expertise on discrete fracture modeling.

Thank you to Albert Genter and Keith Evans for sharing data from the European EGS project at Soultz.

Thank you to my friends for making this year such a great one. Especially to Kelly. We shared so many happy times, and we'll have many more in the future.

Thank you to my parents Dan and Judy, my brother Andrew, my sister Kathleen, my grandparents Keith and Lucy and Larry and Dolores, and my entire family for always being full of love and support. You are my role models.

Funding for this work was provided generously by Google.org.

Contents

| | |
|---|-----|
| Abstract..... | v |
| Acknowledgments..... | vii |
| Contents | ix |
| List of Figures | xi |
| 1.1. Energy and the Environment..... | 1 |
| 1.2. Enhanced Geothermal Systems..... | 1 |
| 1.3. Opportunities for Improvement | 3 |
| 2.1. European EGS Project at Soultz-sous-Forêts, France..... | 7 |
| 2.2. Coulomb Failure | 10 |
| 2.3. Geology of Fracturing..... | 15 |
| 2.4. EGS Stimulation | 21 |
| 2.4.1. Stimulation at Soultz..... | 21 |
| 2.4.2. Critical Stress Analysis at Soultz..... | 26 |
| 2.4.3. A Simple Model of the Effect of Heterogeneity | 32 |
| 3.1. Effective Continuum vs. Discrete Fracture Modeling | 35 |
| 3.2. Previous Work | 36 |
| 3.3. DFN Static Model..... | 37 |
| 3.3.1. Golder FracMan | 37 |
| 3.3.2. Static Model Generation | 38 |
| 3.4. Hydro-Thermo-Mechanical DFN Simulation..... | 41 |
| 3.4.1. Overall Modeling Strategy..... | 41 |
| 3.4.2. Mass Balance | 42 |
| 3.4.3. Energy Balance | 44 |
| 3.4.4. Boundary Element Method for Elastostatics..... | 45 |
| 3.4.5. Displacement Discontinuity Method | 50 |
| 3.4.6. Coulomb Failure and the Displacement Discontinuity Method..... | 52 |
| 3.4.7. Heat Conduction in the Volume | 53 |
| 3.4.8. Thermoelasticity..... | 57 |
| Nomenclature..... | 61 |
| References..... | 65 |
| A. Einstein Notation | 73 |

List of Figures

| | |
|--|----|
| Figure 1-1: Schematic of an EGS system. Reproduced from Tester et al. (2007). | 3 |
| Figure 2-1: Normalized frequency histogram of aperture size for mode I and mode II fractures in EPS1. There are 2213 mode I fractures and 780 mode II fractures. Data supplied by GEIE Exploitation Minière de la Chaleur. Methodology described in Genter (1996). | 9 |
| Figure 2-2: Maximum frictional strength for a variety of rocks at relatively low stresses. Reproduced from Byerlee (1978). | 14 |
| Figure 2-3: Modes of fracture. Reproduced from commons.wikimedia.org. | 15 |
| Figure 2-4: Fault in sandstone. Picture taken by the author of an outcrop in Red Rock Canyon State Recreation Area, Kern County, CA. | 16 |
| Figure 2-5: Process of strike-slip fault formation through linkup of preexisting fractures. Reproduced from Martel (1990). | 17 |
| Figure 2-6: Splays fractures forming off a vertical fracture slipping in the strike slip direction. Mode II splays form off the sides and mode III splays form off the top. Reproduced from Martel and Boger (1998) with modification. | 18 |
| Figure 2-7: Formation of a fault zone between two adjacent slip planes. Reproduced from Segall and Pollard (1983) with modification. | 19 |
| Figure 2-8: Formation of a cavity at a fault step-over. Reproduced from Segall and Pollard (1983). | 20 |
| Figure 2-9: UBI image log and wellbore cross-sectional area from a sheared fracture in GPK1. Reproduced from Evans et al. (2005a). | 22 |
| Figure 2-10: GPK1 borehole shape at 2858.29m before and after stimulation. Reproduced from Evans et al. (2005a). | 23 |
| Figure 2-11: Flow and temperature logs from GPK1 post-stimulation. Permeable fractures are shown. Reproduced from Bachler et al. (2000). | 24 |

| | |
|--|----|
| Figure 2-12: Reproduced from Henriksen (2001). Henriksen interpreted the aperture of the fractures and used qualitative flow data and temperature logs interpreted by Bachler et al. (2000)..... | 25 |
| Figure 2-13: Flow log of GPK3. Reproduced from Baria (2004)..... | 26 |
| Figure 2-14: Mohr diagram with permeable fractures before and after stimulation of GPK1. Reproduced from Bachler et al. (2000)..... | 28 |
| Figure 2-15: Mohr diagram of non-permeable fractures before and after stimulation of GPK1. Reproduced from Bachler et al. (2000)..... | 28 |
| Figure 2-16: Radial pressure distribution in an isolated, infinite fracture after three days of constant pressure injection for different values of permeability..... | 31 |
| Figure 2-17: Random fracturing | 33 |
| Figure 2-18: Prioritized fracturing | 33 |
| Figure 2-19: Flow rate through a “prioritized fracturing” model..... | 34 |
| Figure 3-1: DFN Generated in FracMan..... | 38 |
| Figure 3-2: Overall modeling algorithm | 42 |
| Figure 3-3: Discretization in BEM..... | 45 |
| Figure 3-4: Triangular coordinate system..... | 49 |

Chapter 1

1. Introduction

1.1. Energy and the Environment

The energy and environmental challenges faced by the United States and the world are well known. From 1990 to 2006, global consumption of electricity grew 57% and consumption of crude oil grew 27%. Developing countries are growing rapidly, creating tremendous increase in demand for energy. From 1990 to 2006, China's electricity consumption increased 360%, and crude oil consumption increased 215%. The growth is not limited to developing countries. From 1990 to 2006, the United States increased its electricity consumption 35% and its crude oil consumption 22% (Energy Information Administration).

The past twenty years has also seen a growing consensus in the scientific community that human greenhouse gas emissions such as CO₂ cause severe disruption of global climate. According to Intergovernmental Panel on Climate Change's 2007 report, "[w]arming of the climate system is unequivocal," and the increase in temperature is "very likely due to the observed increase in anthropogenic GHG concentrations." "Eleven of the last twelve years (1995-2006) rank among the twelve warmest years in the instrumental record of global surface temperature (since 1850)" (IPCC 2007). The rate of emission is accelerating, with the global rate of CO₂ emission rising 35% from 1990 to 2006 (Energy Information Administration).

The conflicting goals of increasing global energy supply and reducing emissions are poised to create tremendous demand for energy sources that do not emit greenhouse gasses. There is a major incentive to develop technologies which can produce energy safely, at low cost, and with low emissions.

1.2. Enhanced Geothermal Systems

Geothermal energy has been used for electricity generation since 1904 when a 10 kW generator was installed at the Lardello dry steam field in Italy. Since then, geothermal energy use has spread across the globe. In 2004, geothermal energy produced 54,793 GW-hr of electricity worldwide (Lund, 2004). Depending on the design of the power plant, geothermal power plants emit either very low or zero greenhouse gasses. Geothermal plants provide extremely reliable, base load electricity. Cost is competitive with fossil fuel energy sources. Sanyal (2005) estimated the levelised cost of a 50 MW geothermal power plant between 3.6 and 4.1 ¢/kW-hr.

Despite its advantages, adoption of geothermal energy has been limited. Geothermal energy accounts for around 0.3% of global electricity production. The problem is that there are a limited number of locations on earth where geothermal energy is geologically viable. A geothermal field needs (1) heat, (2) water, and (3) permeability (ability for water to flow through the rock).

Enhanced Geothermal Systems (EGS) have been proposed as a way to dramatically increase the number of locations where geothermal energy can be produced (Tester et al. 2006). At depths within conventional drilling range, the Earth's temperature is hot enough to produce geothermal electricity across a significant percentage of the United States. The difficulty is that at great depth rock is typically crystalline bedrock with little natural permeability.

The EGS concept is to pump water down at high pressure in order to fracture the rock. The fractures form conduits to flow, creating a man-made geothermal reservoir.

Fracturing has been used in oil and gas for decades as a way to improve productivity of wells. The technology continues to develop. In the past fifteen years, new fracturing techniques were developed that enabled production of vast, previously uneconomic natural gas in low permeability shale formations such as the Barnett Shale in Texas. Natural gas production from the Barnett Shale increased from 28 billion standard cubic feet in 1997 to 1098 billion standard cubic feet in 2007 (Railroad Commission of Texas, 2008). The improvement in fracturing technology affected the domestic and global natural gas market profoundly.

EGS was first attempted in the 1970s at Fenton Hill, New Mexico when a team of researchers sponsored by the Department of Energy demonstrated the viability of the technique. Since then, EGS reservoirs have been created in England, France, Germany, Japan and Australia, among others (Tester et al., 2007). The typical strategy has been to drill a well, fracture it hydraulically, and then drill another well into the region where the rock was fractured. Cool water is injected in one well, heats up as it flow through the rock, and is produced from the other well. This is illustrated schematically in Figure 1-1.

The potential of EGS is great. A report issued by a team of geothermal experts assembled by MIT (Tester et al., 2007) concluded that the total US resource base of EGS would be around 14 million exajoules (EJ). One exajoule is 10^{15} Joules. Given their most conservative assumptions about recovery efficiency, the report estimated that the extractable energy available in the US is around 300,000 EJ. The annual consumption of primary energy in the US is roughly 100 EJ. Tester et al. (2007) estimated it would require an investment of \$300 to \$400 million over 15 years to make early generation EGS cost-competitive.

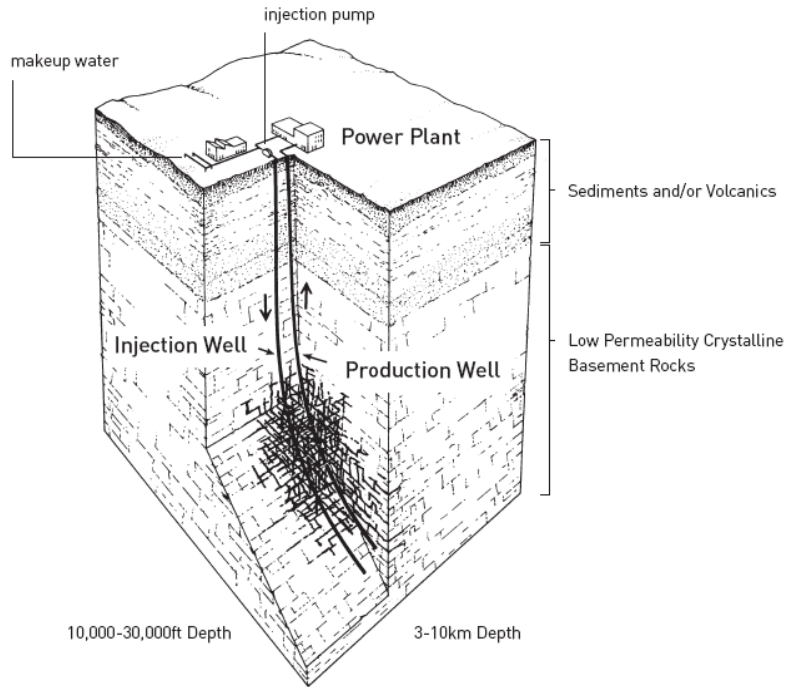


Figure 1-1: Schematic of an EGS system. Reproduced from Tester et al. (2007).

1.3. Opportunities for Improvement

It has been proven that EGS is technically feasible, the resource base exists, and that it is easy to find. The remaining challenge is economic. EGS wells have not been sufficiently productive to justify the expense of drilling deep wells. One solution would be to reduce costs, perhaps through improved drilling technology. The alternative to lowering cost is to increase revenue. This research has focused on the latter.

The amount of electricity produced per well is directly related to the temperature of the produced fluid and the flow rate. EGS wells have achieved flow rates in the range of 20-40 kg/sec. To make EGS economic on a large scale, flow rates in the range of 50-100 kg/sec should be the goal. Given modest assumptions, namely a temperature drop in the power plant of 150°C and turbine efficiency of 10%, 100 kg/sec of liquid water would yield about 6 MW of electricity. Sold at 5¢ per kW-hr, such a plant would generate \$2.6 million income per year.

Maintaining the temperature of the produced fluid is another important issue. Because the reservoir is fractured, there may be a small number of major conduits to flow between the injector and producer. If so, the rock immediately surrounding those conduits could cool down, and cool fluid could be produced at the producer in a relatively short period of time. This would occur even though the vast majority of the rock between the two wells would remain at high temperature. This phenomenon is referred to as “short circuiting.”

Short circuiting occurred at the EGS project at Hijiori, Japan, where produced temperature dropped from 163° to 100° over two years (Tester et al., 2007). Short-circuiting of injected fluids is always a concern in fractured reservoirs, including conventional geothermal fields and secondary recovery in fractured oil and gas reservoirs.

A third challenge is to ensure that a good connection can be achieved between the injector and producer. There have been EGS projects where wells were successfully stimulated, but the connection achieved between them was poor. An example is the Ogachi project in Japan (Tester et al., 2007).

A fourth challenge is induced seismicity. The stimulation process causes microseismic events. They are very small earthquakes on the order of one or two on the Richter scale. The largest ever caused by an EGS project was at Basel, Switzerland, with magnitude 3.4. The largest of these events have been felt at the surface and caused minor property damage. The news media has stoked fears of EGS stimulation causing a large, damaging earthquake (Glanz, 2009a). Fears about induced seismicity are currently threatening a project at the Geysers in Northern California (Glanz, 2009b) and caused the cancellation of the project in Basel (Tester, 2007). At the very least, induced seismicity frightens and annoys local residents. For these reasons, induced seismicity has become an important subject to study.

These four issues (flow rate, short circuiting, interwell connectivity, and induced seismicity) are all controlled by the process of hydraulic fracturing. Increasing the hydraulic conductivity of the fractures between wells would increase flow rate. Increasing the number of conductive fractures between wells would increase flow rate and prevent short circuiting. A better understanding of the fracture process would improve efforts to ensure connection between two wells and constrain effects of induced seismicity.

EGS projects are possible in some sedimentary formations, but they are most likely to be found in crystalline bedrock formations. Therefore, stimulation in EGS is different than in oil and gas because oil and gas reservoirs are almost always in sedimentary rock. Because there has been much less research on fracturing in crystalline rocks, the process is not as well understood.

There are two possible mechanisms of hydraulic fracturing. In one, hydraulic fracturing forms a new fracture which opens up and propagates away from the wellbore. In the other, preexisting fractures, possibly sealed shut by hydrothermal alteration, slip as the increase in fluid pressure lessens fractures' frictional resistance to shear. After slip, fracture conductivity can be increased by orders of magnitude.

Fracture stimulations could occur by either process or both. In general, the former mechanism is more likely to occur in sedimentary formations, and the latter is more likely to occur in crystalline formations. Because it is more relevant to oil and gas, the former

process has been the subject of much more research than the latter. However the latter is more relevant to EGS application.

There are two factors controlling stimulation through shear of preexisting fractures: (1) the preexisting fracture network and (2) the process by which the hydraulic stimulation propagates into the network and stimulates conductivity. In addition, fractures could open due to pressure or thermoelastic effects. Fracture opening would result in greatly increased flow rate, and would change dynamically during the life of the reservoir.

This report is focused on describing an investigation of these factors. There is a discussion of the natural processes that create fractured rock. This was studied from a geological and a rock mechanics perspective. The European EGS project at Soultz-sous-Forêts, France has an outstanding, publicly available dataset, and it has been used as an example of a typical EGS project. The project is reviewed here, and their experience of EGS stimulation is discussed.

The second half of the report is concerned with modeling of stimulation. Coupled with a conceptual understanding of what is happening in the reservoir, computer modeling offers tremendous power to describe the process of stimulation. This report lays out in detail how to construct an EGS stimulation model. Topics include geometry of the unstimulated reservoir, mass and energy transport, elastostatics, Coulomb frictional failure, and thermoelasticity. Finite difference, boundary element, and analytical solutions are used where appropriate.

Applications of EGS stimulation modeling are numerous. They include (1) investigation of novel strategies for stimulation design, (2) optimization of wellbore orientation and spacing, (3) prediction of thermal breakthrough, (4) sensitivity study on the effect of different parameters, (5) prediction of intensity and location of microseismic events, and (6) identification of geological settings that are advantageous for EGS.

Chapter 2

2. Application of Rock Mechanics to EGS

2.1. European EGS Project at Soultz-sous-Forêts, France

The European EGS Project located at Soultz is a good case study because it has high quality, publicly available data.

The project is located in the Upper Rhine Graben in northeastern France. Roughly 1.4km of Cenozoic and Mesozoic sediment overlay the crystalline basement, which is porphyritic granite. The temperature at 3.5km is roughly 150°C and at 5km roughly 200°C.

From 1991-1997, two wells (GPK1 and GPK2) were drilled and stimulated at a depth of 3.5km. A four month circulation test was carried out between the wells. From 1999-2004, GPK2 was deepened and two more wells (GPK3 and GPK4) were drilled to a depth of 5km, and they were stimulated between 2000 and 2007. At depth, the wells are about 700m apart, and they are uncased for the bottom 500m. In 2005 a five month circulation test was carried out between the injector, GPK3, and the two producers GPK2 and GPK4 (Genter, 2009).

Extensive logging tools have been run during every phase of the operation. In addition, the shallow well EPS1 was cored from 930m to 2230m (Genter, 1996). Observation wells were used to locate microseismic events occurring during the stimulations.

During the 1997 flow test between GPK1 and GPK2, a flow rate of about 25 kg/sec was achieved. The injection pressure was 2-4 MPa, and a submersible pump installed in the producer GPK2 (Baumgartner 1998). During a flow test from GPK3 to the deepened GPK2, a flow rate of roughly 30 kg/sec was maintained with an injection pressure of 10 MPa and a suction pressure of 5 MPa (Tischner, 2006).

Tracer results in both the shallow and deep reservoirs indicated there was roughly a 30% return of injected fluid, indicating that the stimulated reservoir is open to a larger hydrothermal system with exchange of fluid in and out (Genter, 2009). This indicates that at least some preexisting fractures have conductivity. A tracer test between GPK2 and GPK3 showed returns after four days and peaked from 11-17 days. Sanjuan (2007) used the test to estimate that there was a relatively short, conductive pathway between the two wells that took 70% of flow with a swept volume of 3900m³. All other pathways between the wells are collectively less conductive and constituted roughly 6500m³ of swept volume.

Values of *in situ* stress state are available from hydrofracture stress measurements, image logs of wellbore failure, density logs, and focal mechanisms of microearthquakes caused by stimulation. The most recent assessment of *in situ* stress state is available from Valley and Evans (2007). This study provided the following expressions for the state of stress at Soultz as a function of depth, given in MPa:

$$S_v = -1.30 + 25.50z(km) \quad (2-1)$$

$$S_{h_{min}} = -1.78 + 14.06z(km) \quad (2-2)$$

$$-1.17 + 22.95z(km) \leq S_{H_{max}} < -1.37 + 26.78z(km) \quad (2-3)$$

$$P = 0.9 + 9.8z(km) \quad (2-4)$$

The orientation of $S_{H_{max}}$ is given as N169°E±14°, which is consistent with the site's location on the western edge of a graben that is forming by E-W extension.

To explain what these values mean, the state of stress can be expressed in terms of values in three orthogonal principal directions. In the subsurface, one principal direction, S_v , is typically assumed to be vertical (although this is not always the case). The other two, $S_{h_{min}}$ and $S_{H_{max}}$, are usually assumed to be horizontal. Equation 2-4 gives the hydrostatic pressure gradient.

Most fractures at Soultz belong to one of two steeply dipping fracture sets. One dips to the east and the other to the west. The fractures strike roughly N-S. The fracture spacing is not regular. Instead fractures tend to cluster together in zones. Depending on the depth and method of observation, different values of fracture spacing are available, but they tend to be on the order of 0.5-1 fracture per meter (Dezayes, 2005).

Based on the EPS1 core, Genter (1996) reported that composition of the fracture infilling. The most common minerals were quartz, hematite, calcite, and illite. Illite and quartz were more common in the larger aperture fractures and calcite was most common in the smaller fractures. Hematite was present in only two zones: the upper two zones of heavy fracture density. Other minerals present were dolomite, chlorite, epidote, barite, pyrite, and galena. There was alteration to the granite around some of the fracture clusters, especially the ones where quartz, hematite, and illite were found. Roughly 30 of the 3300 fractures had partial cementation. The rest were completely cemented. Completely cemented fractures have no apparent transmissibility while some partially cemented fractures demonstrate some low transmissibility. Evans et al. (2005a) report that 18 fractures demonstrated some transmissibility in GPK1.

Genter (1996) interpreted each fracture in the EPS1 core as being either mode I (opening) or mode II or III (shear) fracture. The distinction is made based on whether or not any

displacement is observed along the fracture in the plane of the fracture. Large aperture fractures were almost exclusively shear fractures, as seen in Figure 2-1.

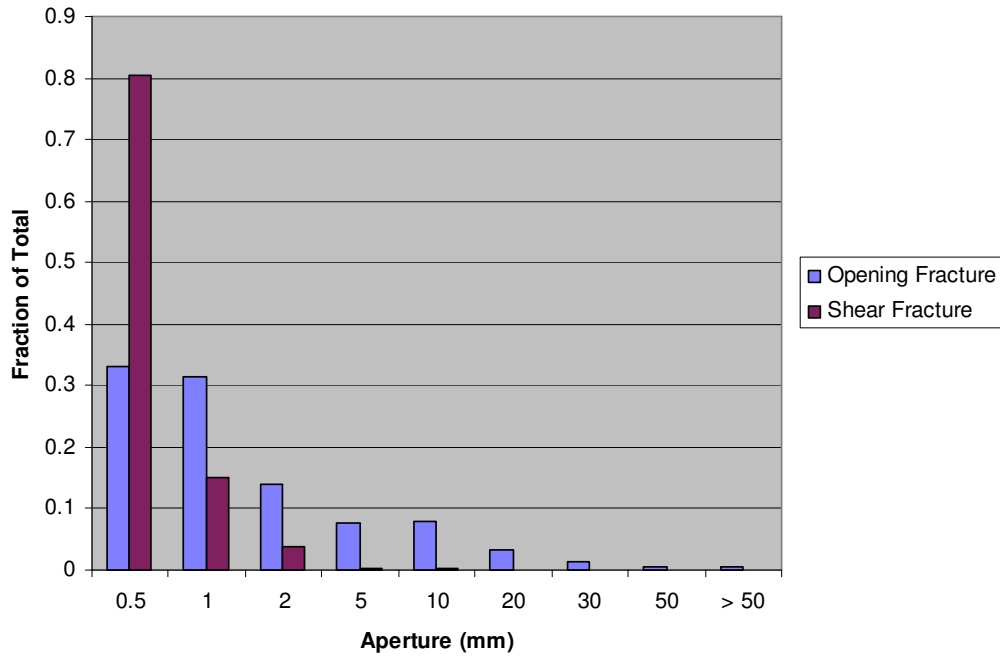


Figure 2-1: Normalized frequency histogram of aperture size for mode I and mode II fractures in EPS1. There are 2213 mode I fractures and 780 mode II fractures. Data supplied by GEIE Exploitation Minière de la Chaleur. Methodology described in Genter (1996).

It is generally observed that higher aperture fractures display a larger transmissibility. The classic correlation is the cubic law, which states that the flow rate in a fracture is proportional to the cube of its hydraulic aperture (Jaeger et al., 2007). The hydraulic aperture is the width of the opening in the core that is available to flow. However this correlation can be misleading because hydraulic aperture is not what is typically observed in practice. Few of the natural fractures observed in EPS1 and the other Soultz wells had any apparent free aperture, and they all had very low transmissibility. Instead the aperture was measured as the width of the hydrothermal deposits and the crushed and mineralized zone around the core. This is what is shown in Figure 2-1. Therefore there would not necessarily be a correlation between observed aperture and fracture transmissibility.

It was observed that during the stimulations a microseismic cloud developed around the injector roughly in an ellipsoid with the long axis aligned in the direction of maximum horizontal stress. During the stimulation of the deep wells GPK2 and GPK3, about 400 events greater than 1 M_L (M_L is the Richter scale) were measured; about 30 were measured over 2 M_L and the largest was 2.9 M_L (Baria, 2005). Microseismic focal mechanisms typically indicated mixed strike slip and normal faulting (Cornet, 2007).

During stimulation of the shallower wells GPK1 and GPK2, roughly 9 MPa of overpressure was needed (Bachler, 2000). Overpressure is the increase in pressure of the formation at the wellbore above the natural formation pressure during injection. After deepening to 5km, GPK2 required up to 13 MPa of overpressure. GPK3 required 16 MPa (Cuenot et al., 2006). GPK4 required 17 MPa of overpressure (Baria et al., 2006).

2.2. Coulomb Failure

The fractures at Soultz are stimulated when increasing pore pressure in their core reduces the effective normal force on the fracture plane, allowing them to slip. Depending on parameters such as the type of rock, slip on a fracture could increase or decrease permeability. In the case of crystalline rock, both field experience and laboratory experiments verify that when a fracture slips, conductivity increases, possibly by orders of magnitude. This has been observed in a variety of rock types including Austin chalk (Olsson, 1993), Permian sandstone (Yeo, 1998), and granite (Chen, 2000, Osaki, 1999). A variety of mechanisms may be at work. One mechanism may be the breaking up chemical precipitation that is sealing the fracture. Another is the creation of mismatches in the microscale aperture variations on the fracture surface (Auradou, 2006).

The classic Coulomb failure criterion is used to predict when a fracture will fail in shear (Jaeger et al., 2007). It is assumed the shear stress acting on the fracture plane, τ , is resisted by friction which is proportional to the normal stress, σ_n . The fracture will slip if the shear stress on the fracture exceeds the ability of friction to resist it. The ability to resist slip is equal to σ_n multiplied by the coefficient of friction, μ . There is an additional term S_o , called the cohesion, because even at zero normal stress some nonzero shear force may be required to initiate sliding. The fluid pressure, P , in the fracture has the effect of reducing the normal stress but has no effect on the shear stress. The effective normal stress, σ'_n , is defined as:

$$\sigma'_n = \sigma_n - P \quad (2-5)$$

The result is the Coulomb failure criterion, an expression that failure will occur if the following equation is satisfied:

$$|\tau| = S_o + \mu\sigma'_n \quad (2-6)$$

The stress at a point in space is given by the 3x3 stress tensor, \mathbf{T} . There are nine values in the tensor, but it is symmetrical, so that there are six independent values that fully define the state of stress at a point. The tensor is given as:

$$\mathbf{T} = \begin{bmatrix} \sigma_{xx} & \sigma_{yx} & \sigma_{zx} \\ \sigma_{xy} & \sigma_{yy} & \sigma_{zy} \\ \sigma_{xz} & \sigma_{yz} & \sigma_{zz} \end{bmatrix} \quad (2-7)$$

where $\sigma_{xy} = \sigma_{yx}$, $\sigma_{xz} = \sigma_{zx}$, and $\sigma_{yz} = \sigma_{zy}$. Given an arbitrarily oriented plane in space given by the unit normal vector \mathbf{n} , the traction on that plane \mathbf{p} is given as:

$$\mathbf{p} = \mathbf{T}\mathbf{n} \quad (2-8)$$

Written out completely, it is:

$$\begin{bmatrix} p_x(\mathbf{n}) \\ p_y(\mathbf{n}) \\ p_z(\mathbf{n}) \end{bmatrix} = \begin{bmatrix} \sigma_{xx} & \sigma_{yx} & \sigma_{zx} \\ \sigma_{xy} & \sigma_{yy} & \sigma_{zy} \\ \sigma_{xz} & \sigma_{yz} & \sigma_{zz} \end{bmatrix} \begin{bmatrix} n_x \\ n_y \\ n_z \end{bmatrix} \quad (2-9)$$

The normal traction on the plane is found by projecting \mathbf{p} onto \mathbf{n} :

$$\sigma_n = \mathbf{p} \cdot \mathbf{n} \quad (2-10)$$

The Pythagorean theorem gives the magnitude of the shear stress (Jaeger et al., 2007):

$$\tau^2 = |\mathbf{p}|^2 - \sigma_n^2 \quad (2-11)$$

The orientation of the shear stress can be calculated by projecting the traction vector onto the plane. Given two nonparallel vectors in the plane, \mathbf{a}_1 and \mathbf{a}_2 , define a matrix \mathbf{A} with its columns being the vectors \mathbf{a}_1 and \mathbf{a}_2 . The vectors \mathbf{a}_1 and \mathbf{a}_2 can be found by setting their dot product with \mathbf{n} equal to zero and arbitrarily choosing two of their three values. The projection of a vector onto the plane is given by (Strang, 2006):

$$proj_{\mathbf{A}}(\mathbf{p}) = \mathbf{A}(\mathbf{A}^T \mathbf{A})^{-1} \mathbf{A}^T \mathbf{p} \quad (2-12)$$

Often the Coulomb failure criterion is used to predict failure of rock in which there is not a preexisting flaw. This is based on laboratory experiments in which unfractured rock samples are loaded in compression until failure. Under most loading conditions, the failure occurs by the spontaneous formation of a shear fracture out of the previously unfractured rock. In that case, Coulomb theory could be used to predict the orientation of the plane of failure. Coulomb failure is just one of many theories that can be used to predict the orientation of the plane of failure. The physical mechanism of failure is not addressed by Coulomb theory and is the subject of much discussion in the rock mechanics literature, which will not be elaborated upon here. This application of Coulomb failure is not used in this paper because formation of new shear fractures in unfractured rock is not believed to mechanism of EGS fracture stimulation. However it is mentioned for completeness.

For failure in unfractured rock, the plane of failure will be in the optimal orientation, and the failure criterion can be expressed in terms of the two principal stresses σ_1 and σ_3 (Jaeger et al., 2007):

$$\sigma_1 = 2S_o \tan \beta_f + \sigma_3 \tan^2 \beta_f \quad (2-13)$$

where:

$$\beta_f = 45^\circ + 1/2 \tan^{-1} \mu \quad (2-14)$$

A representative failure envelope for a rock sample of unfractured granite is (Haimson, 1995):

$$\sigma_1 = 192 + 11.3\sigma_3 \text{MPa} \quad (2-15)$$

This equation is from a “triaxial” compression test in which a cylindrical sample was placed in a sleeve and the radial stress was kept constant at σ_3 (so $\sigma_2 = \sigma_3$) as the axial compression, σ_1 , was increased until failure. Evidence in the literature suggests that if the intermediate stress, σ_2 , is higher than σ_3 , then the σ_1 required for failure is even higher. This contradicts the Coulomb failure criterion. This contradiction and others have led to a variety of alternative criteria for compressive failure to be proposed. For examples see Haimson (1995) or Jaeger et al. (2007). This issue does not need to be considered further because this report is mainly concerned with the failure of preexisting fractures.

In this paper, the Coulomb criterion is applied to individual preexisting fractures with a defined orientation. The mechanism of shear failure on a preexisting flaw allows for easy physical explanation. Shear failure is equivalent to sliding two boards past one another while simultaneously pressing them together.

This distinction is worth pointing out because often values of μ and S_o are quoted in the literature for various types of rock. These values are typically calculated from laboratory testing of unfractured rock. The physical mechanism of that kind of failure is different from failure of a preexisting fracture, and so the values of μ and S_o are not necessarily applicable.

Laboratory testing has been performed on rock samples with preexisting fractures. Byerlee (1967) performed triaxial compressive tests on samples of granite with polished surfaces and saturated with water for values of σ' from 200-1000 MPa and fit his data to the equation:

$$|\tau| = 10 \text{MPa} + 0.6\sigma'_n \quad (2-16)$$

Byerlee (1967) tested dry samples and fitted his results for both polished surface and rough surface to the same equation:

$$|\tau| = 50 \text{MPa} + 0.6\sigma'_n \quad (2-17)$$

Byerlee (1967) also observed that the frictional coefficient changed with displacement. In the case of polished surfaces, friction increased, peaked, and then decreased. That is probably an artifact from the polished surfaces coming in full contact with one another. For the rough mated surfaces, μ declined monotonically with displacement, starting near 0.6, but eventually approaching 0.5. It is common to observe on fractures that after initial failure, the coefficient of friction decreases.

Barton (1976) collected results from Byerlee's rock testing from different kinds of rock: Westerly granite, Solenhofen limestone, Oak Hall limestone, Nahant gabbro, Spruce Pine dunite, Cabamurra serpentinite, and Weber sandstone. Barton observed at high effective stress, the failure criterion for the different rock types fell reasonably close to one another. Later, Byerlee (1978) proposed a simple expression for frictional strength at high stresses:

$$|\tau| = 0.85\sigma'_n \quad \text{for } \sigma'_n < 200\text{MPa}$$

$$|\tau| = 50\text{MPa} + 0.85\sigma'_n \quad \text{for } 200 < \sigma'_n < 1700\text{MPa} \quad (2-18)$$

This expression is so well known it is sometimes called Byerlee's Law (Jaeger et al., 2007). Byerlee also observed that the data scatter was relatively small and did not seem to depend on rock type.

It must be stressed that these results were only applicable for high values of stress. Barton and Byerlee both reported that at low stresses, data showed a great deal of scatter and generalizations were not possible. Byerlee searched the literature for fracture frictional failure tests at 5 MPa or less and found that depending on the experiment, estimates of μ varied from 0.3 to 10 (assuming cohesion was zero). This is illustrated in Figure 2-2, which is reproduced from Byerlee (1978).

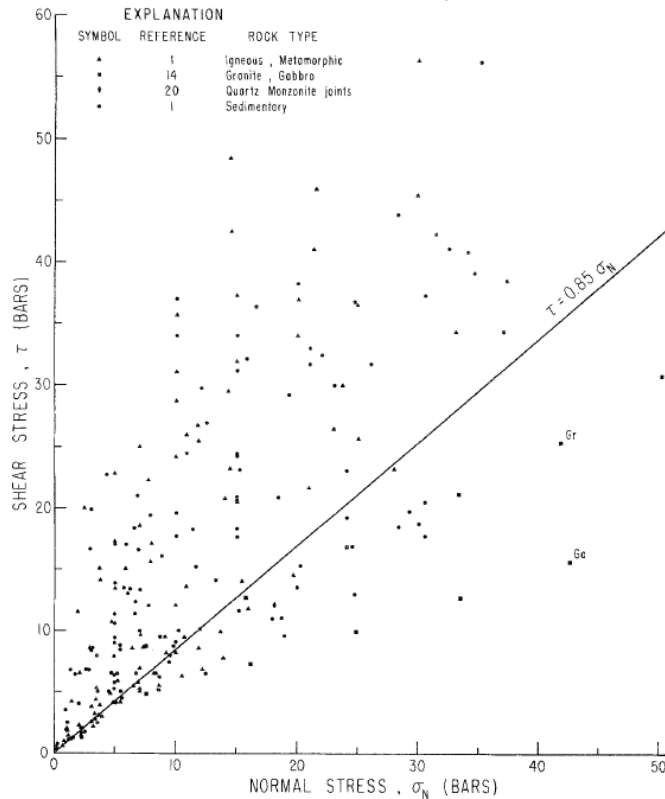


Figure 2-2: Maximum frictional strength for a variety of rocks at relatively low stresses. Reproduced from Byerlee (1978).

Barton related the variation in frictional strength to the roughness of the joint, the compressive strength of the joint, and the “friction angle” of the rock. Other studies have observed that cementation increases the frictional strength of a fracture, but as the thickness increases, the strength decreases (Armand et al., 1998, and Papaliangas, 1995). Armand et al. performed shear tests on calcite-filled joints in granite for normal stresses varying from 5 to 20 MPa and joint apertures from 0.1 to 2mm. Plotting maximum shear stress before failure vs. normal stress, Armand et al. found the values fell between a line of zero cohesion with $\mu=0.9$ and 3.3 MPa cohesion with $\mu=1.35$. Thinner joints had greater frictional strength than thicker joints.

It would be perilous to apply laboratory results to a given field directly, because of the large variance in frictional strength that is observed in different experiments. Variation may be due to a variety of factors, such as rock type and the mineralogy and extent of precipitation. The author is not aware of any laboratory testing that has been done on large aperture fault zones, as opposed to individual small aperture fractures, or if such testing is even technically possible. In conclusion, the evidence suggests that at relatively low pressures, there can be significant variation in the frictional strength of different fractures.

2.3. Geology of Fracturing

Because fractures are so important in EGS reservoirs, it is worth spending some time to understand the processes that form them.

There are three types of fracture: mode I (opening), mode II (sliding), and mode III (tearing). These are illustrated in Figure 2-3.

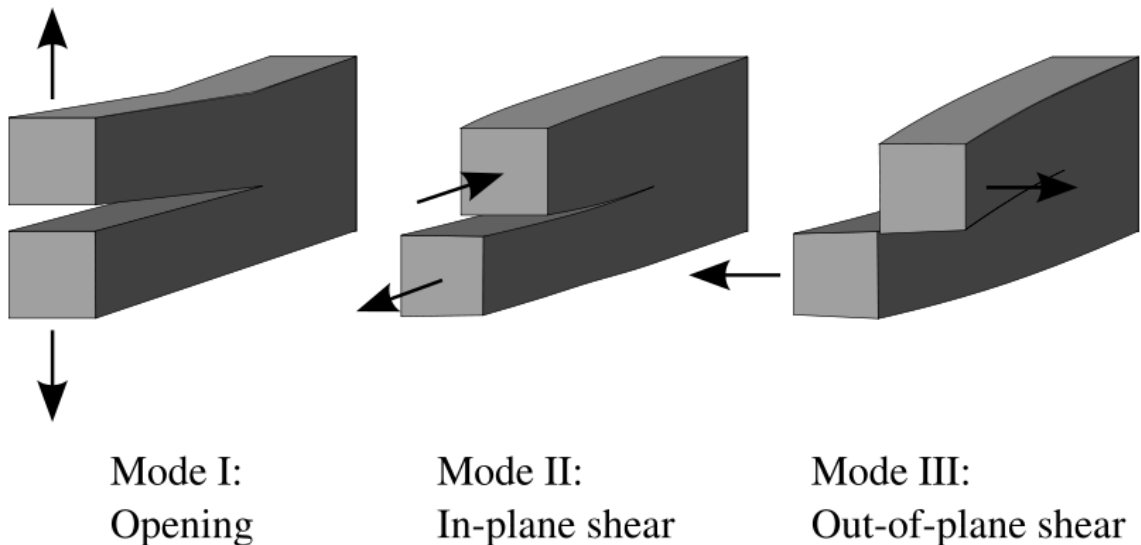


Figure 2-3: Modes of fracture. Reproduced from commons.wikimedia.org.

In this report, “joint” refers to a purely mode I fracture. “Fault” refers to a fracture upon which mode II or mode III displacement has occurred. “Fracture” could refer to either: a discontinuity that formed by one of the modes of failure shown above.

Fractures are found in all kinds of rock. Rock outcrops are observed with only joints (Bankwitz et al., 2004b), only faults (Childs, 1996), or both joints and faults (Segall and Pollard, 1983).

Close examination of faults indicates that there are at least two general mechanisms of faulting in rock. One mechanism is shear failure in previously unfractured rock. The other is failure of preexisting fractures which link up and form larger faults. The preexisting fractures could be joints. These correspond to the two applications of the Coulomb failure criteria mentioned in Section 2.2. The former process appears to be more common in crystalline rock and the latter appears to be more common in sedimentary rock. This is likely because of differences in material properties and apparently indicates that faults form in crystalline rock by a different process than in sedimentary rocks.

As discussed in Section 2.2, when unfractured rock fails in compression, it spontaneously forms a mode II or mode III fracture out of virgin rock. Figure 2-4 shows a picture of a fault in sandstone which formed by shearing through unfractured rock.



Figure 2-4: Fault in sandstone. Picture taken by the author of an outcrop in Red Rock Canyon State Recreation Area, Kern County, CA.

Compressive strength is greater for most crystalline rock is than for most sedimentary rocks. Based on “triaxial” rock tests, a simple shear failure criteria for intact samples of Westerly granite is $\sigma_1 = 192 + 11.3 \cdot \sigma_3$ where σ_1 is the largest compressive stress and σ_3 is the smallest. A similar expression for Darley Dale sandstone is roughly $\sigma_1 = 80 + 5.4 \cdot \sigma_3$ (Jaeger, 2007).

Joints form when the pore pressure exceeds the least compressive stress and the rock experiences an effective tensile stress. Failure occurs when the tensile stress exceeds the tensile strength of the rock, and joints form orthogonal to the direction of least stress. The tensile strength of crystalline rocks is generally greater than in sedimentary rocks, but they are both small compared to compressive strength. Laboratory tests for granite have measured uniaxial tensile strengths for granite from 3-39 MPa and for sandstone 3-7 MPa (Pollard and Fletcher, 2008).

Jointing occurs in granite during cooling of the magma intrusion and due to tectonic stress or high pore pressure (Bergbauer and Martel, 1999, Bankawitz et al., 2004a, Norton et al., 1984, Bankawitz et al., 2004b, Bankwitz, 1994).

As discussed in Section 2.2, the frictional strength of fractures is much less than the compressive strength of virgin rock. If correctly oriented joints already exist in rock, we might expect that they would fail in shear at much lower stresses than would be required

to form new faults out of virgin rock. Evidence in outcrops suggests this is the case, and it is an important mechanism for the formation of faults, especially in crystalline rock.

Two examples of outcrop studies that described this process are Segall and Pollard (1983), who described granite outcrops in the Sierra Nevada in California, and Granier (1985) who described granite outcrops the Massif de la Borne in France.

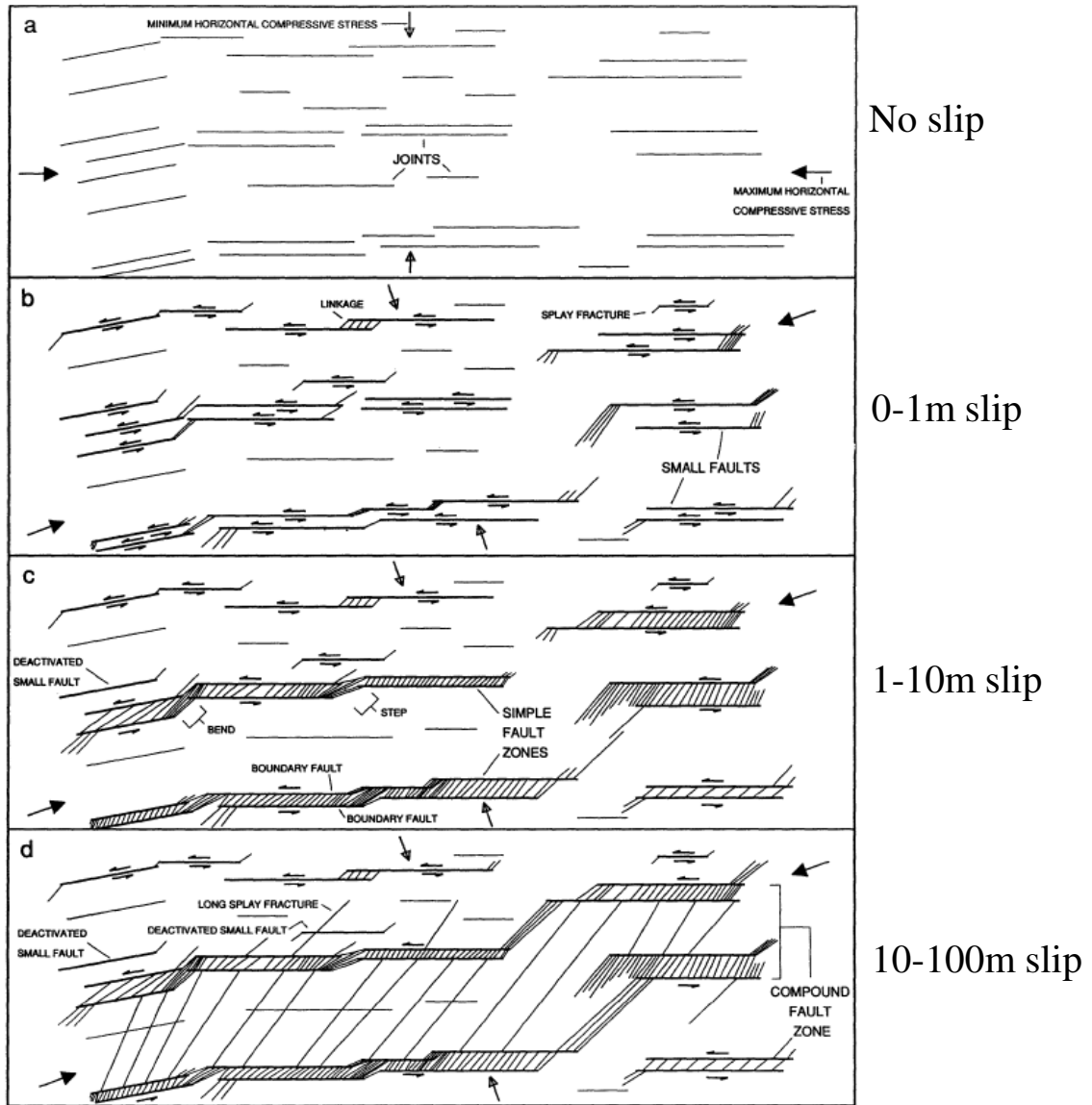


Figure 2-5: Process of strike-slip fault formation through linkup of preexisting fractures. Reproduced from Martel (1990). Labels on the side were added later.

Figure 2-5 illustrates a sequence of steps involved in formation of strike-slip faults viewed from above. An identical sequence of events would form normal faults, but in that case the figure would be rotated 90° and view the sequence from the side.

A shearing fractures experiences both mode II and mode III displacement depending on the side of the fracture. The sense of slip is mode II on the side parallel to slip and mode III on the side perpendicular to slip. This is illustrated in Figure 2-6. If the slip direction is horizontal, mode II slip occurs on the sides and mode III slip occurs on the top and bottom.

On the edges with mode III shear, small fractures twist off the original to form *en echelon* arrays. In an outcrop, the fracture trace would look something like D in Figure 2-6. On the sides with mode II shear, the shear induces tension on two opposite corners of the fracture trace and compression on the other corners. On the corners where tension occurs, secondary fractures called splays propagate away from the original fracture at an angle. The formation of the splays apparently inhibits further growth of the original fracture in its own plane. Splays propagating off the fracture can be seen in C in Figure 2-6.

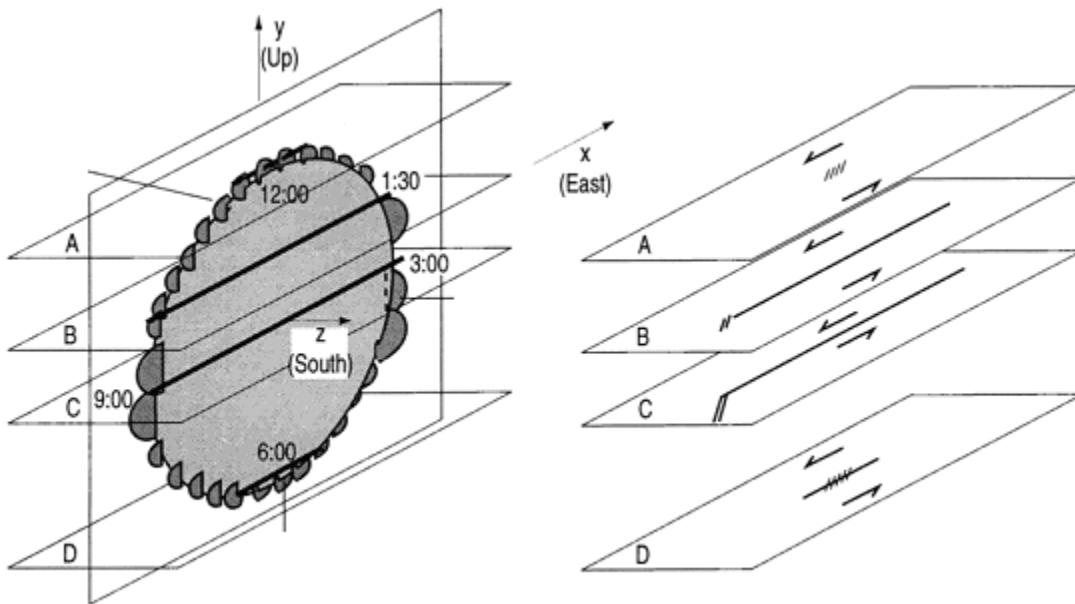


Figure 2-6: Splays fractures forming off a vertical fracture slipping in the strike slip direction. Mode II splays form off the sides and mode III splays form off the top. Reproduced from Martel and Boger (1998) with modification.

The splays will eventually become long enough to reach other fractures and link up. Once the fractures link up, they begin to slip together as if they were a single fault. Faults can grow wider by linking up with adjacent faults. Eventually, a fault zone forms in which slip planes border a cataclased zone. Figure 2-7 is an illustration of a fault zone.

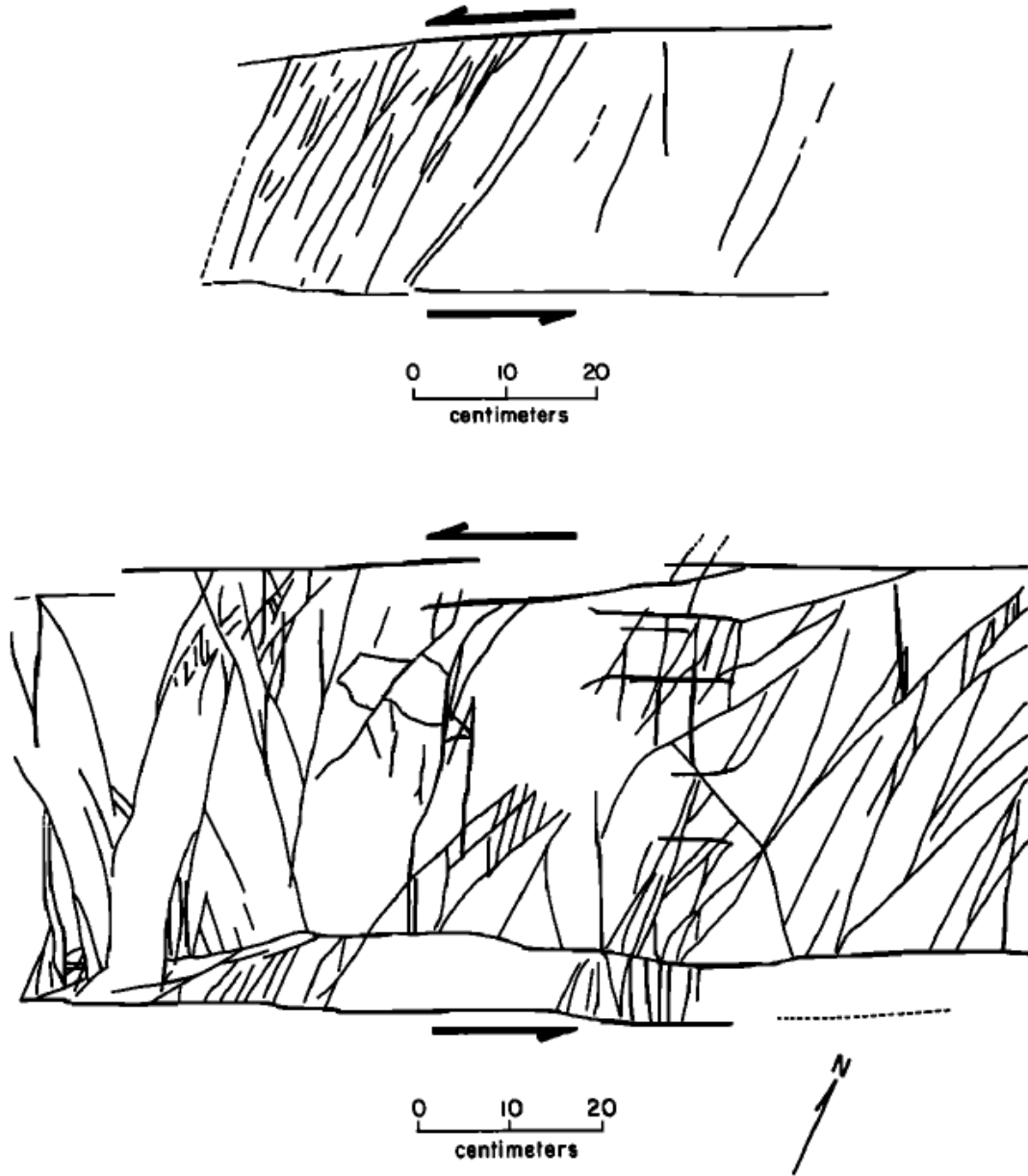


Figure 2-7: Formation of a fault zone between two adjacent slip planes. Reproduced from Segall and Pollard (1983) with modification.

Simple faults could link up with other faults and form compound fault zones.

If faults form by the link-up mechanism described here, it would have far-reaching implications for EGS stimulation.

One consequence is that the orientation of the overall fracture may not be what is seen by a wellbore image log. Consider for example the faults at the bottom of Figure 2-5. They consist of alternating left-right primary fractures and angled splay fracture. If a well were drilled across one of them, the wellbore image log would see either a splay or a primary

fracture. The overall fracture orientation is different from the orientation of either the splays or the primary fractures.

Another interesting consequence may be the existence of channels where there are fracture step-overs. It is very common to observe rhombohedral shaped void opening up at step-overs between the fractures. In outcrop they are usually sealed with hydrothermal filling, which indicates that at one time they were conduits for flow.

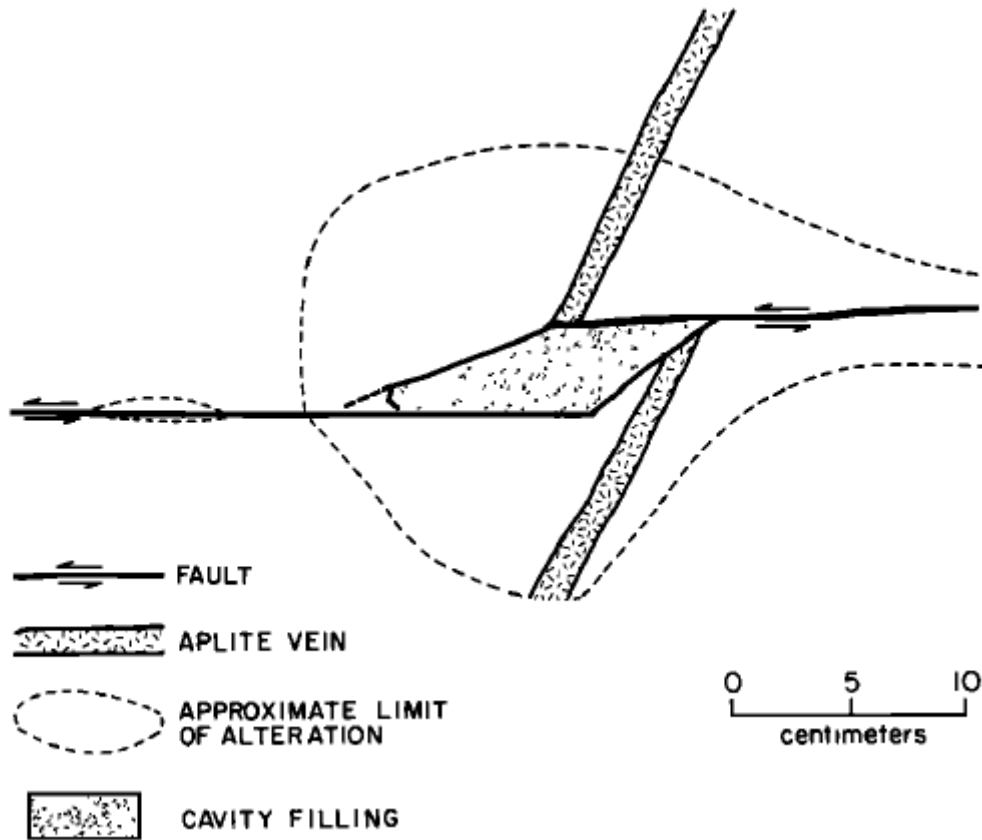


Figure 2-8: Formation of a cavity at a fault step-over. Reproduced from Segall and Pollard (1983).

If these step-overs exist in an EGS reservoir, significant transmissibility anisotropy could result. As discussed in Section 2.4.1, horizontal offset on stimulated fractures at Soultz has been measured directly in the wellbore and is as high as 19 mm. It was not possible to measure the vertical offset on the fractures. The offset could open step-overs that already exist but may be sealed. These cavities would be conduits to flow in the direction perpendicular to the offset.

This possibility has already been mentioned in the EGS literature. For example in Evans et al. (2005c), it is suggested as an explanation for the rapid downward migration of microseismic events during stimulation. It was also proposed by Tezuka and Niitsuma (2000) as a mechanism for stimulation at Hijiori.

There might be consequences for fault aspect ratio. Martel and Boger (1998) point out that splay fractures would tend to be longer and more likely to link up with other fractures where mode II splays form than where mode III splays form. They propose that this process might tend to make normal faults that are taller than they are wide and strike slip faults that are the other way around. It is difficult to test this theory because data on fault aspect ratio in crystalline rock are very scarce. Faults in sedimentary rocks tend to be wider than they are tall, but this can be explained by the mechanical effects of bedding.

The question of what happens at fault intersections is potentially important. For example, do fault cross each other to make “X” shaped intersections, or would one truncate against the other to make a “Y” shaped intersection?

It was observed by Young (2001) in a sedimentary outcrop study that X- and V-shaped fracture intersections were uncommon. If they did appear, they tended to terminate just short of actually intersecting. These “almost” intersections tended to be located in a shale layer, which deforms in a ductile manner and does not fracture. These effects are probably because the stress perturbation of fault slip would tend to inhibit formation of V- or X-shaped intersection. It is much more common in sedimentary rocks to observe a Y-shaped intersection, where one fracture terminates against the other. One interpretation of Y-shaped intersections is that one fault existed first and the other “grew” from it.

What kinds of intersections are common in crystalline rock? Do the intersections fully connect or terminate just short, as observed by Young? It is possible that the core of the intersections could be areas of enhanced or reduced transmissibility. Further study is needed on this topic.

It would be important to keep in mind that the stress state that formed a given fracture set may not be the same as the present stress state.

Overall, it is clearly important to consider what the mechanism for fracture formation in a given EGS reservoir. Many EGS reservoirs have faults, but others might only have joints. The nature of the stimulation in a faulted versus a jointed rock mass is likely to be profoundly different. Appreciation of these differences could allow us to identify the kinds of geologic settings that are optimal for application of EGS stimulation.

2.4. EGS Stimulation

2.4.1. Stimulation at Soutz

Hydraulic stimulation has been used in oil and gas for decades (Economides and Martin 2007). The classic mechanism is that when the wellbore pressure exceeds the least compressive stress, an opening mode tensile fracture forms on opposite sides of the wellbore. The fractures propagate into the formation as long as the pressure is maintained. Proppant is a slurry of sand or other particles that is injected to hold the fracture open after the stimulation ends and pressure returns to the normal (Economides and Martin, 2007).

Observations at Soultz indicate that the dominant mechanism of stimulation is not propagation of tensile cracks away from the wellbore. Transmissibility is created when preexisting fractures fail in shear in the sense of Coulomb failure. Shear enhances the transmissibility by orders of magnitude. Axial tensile fractures are present in the wells at Soultz. However, these fractures do not correlate with increased fluid flow. It is believed they do not extend far from the wellbore (Evans et al., 2005a). Tensile fractures that extend only a short distance from the wellbore are common in oil and gas as well as geothermal. They occur because the stress perturbation of the wellbore creates localized tensile forces. A short distance from the wellbore the perturbation is gone, so the fracture does not propagate into the formation (Zoback, 2007).

Direct observations in the wellbore demonstrate that fractures are shearing and that the sheared fractures have enhanced transmissibility. UBI image logs show changes in the reflectivity of fractures that have been stimulated, indicating damage. The borehole cross-sectional area increases around stimulated fractures. Reconstructions of the borehole shape clearly indicate that shear occurs. Figure 2-9 and Figure 2-10 demonstrate examples of these observations in a representative fracture.

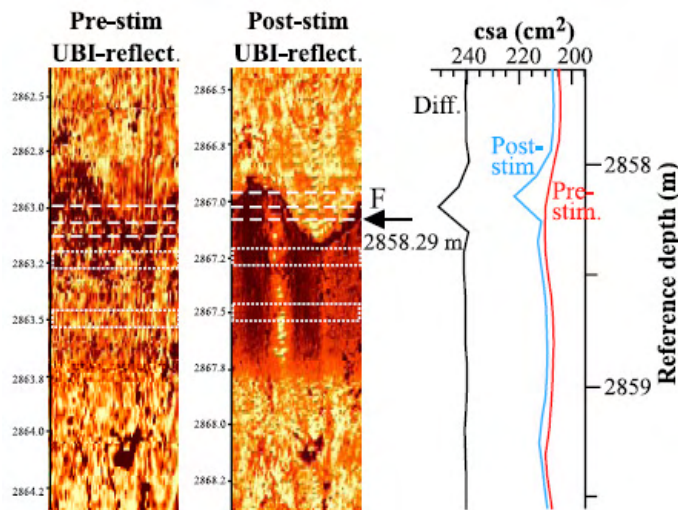


Figure 2-9: UBI image log and wellbore cross-sectional area from a sheared fracture in GPK1. Reproduced from Evans et al. (2005a).

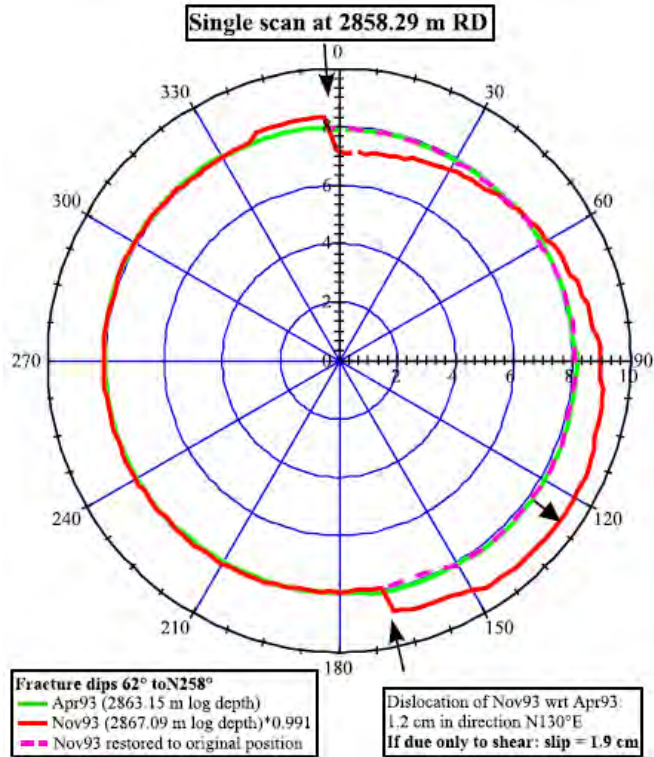


Figure 2-10: GPK1 borehole shape at 2858.29m before and after stimulation. Reproduced from Evans et al. (2005a).

Using spinner logs and temperature logs, the location of inflowing fractures can be determined. It was observed in GPK1 that 95% of the flow occurred through ten fractures. The newly permeable fractures were mainly clustered around these major fractures. Flow was concentrated in six major zones, illustrated in Figure 2-11. The estimated horizontal offset on these major flowing zones following stimulation varied between 2mm and 19 mm (Evans et al., 2005b). It was not possible to calculate the vertical offset from the data.

Figure 2-11 shows flow and temperature logs from GPK1 following stimulation as well as marking the location of every single fracture that showed conductivity following stimulation.

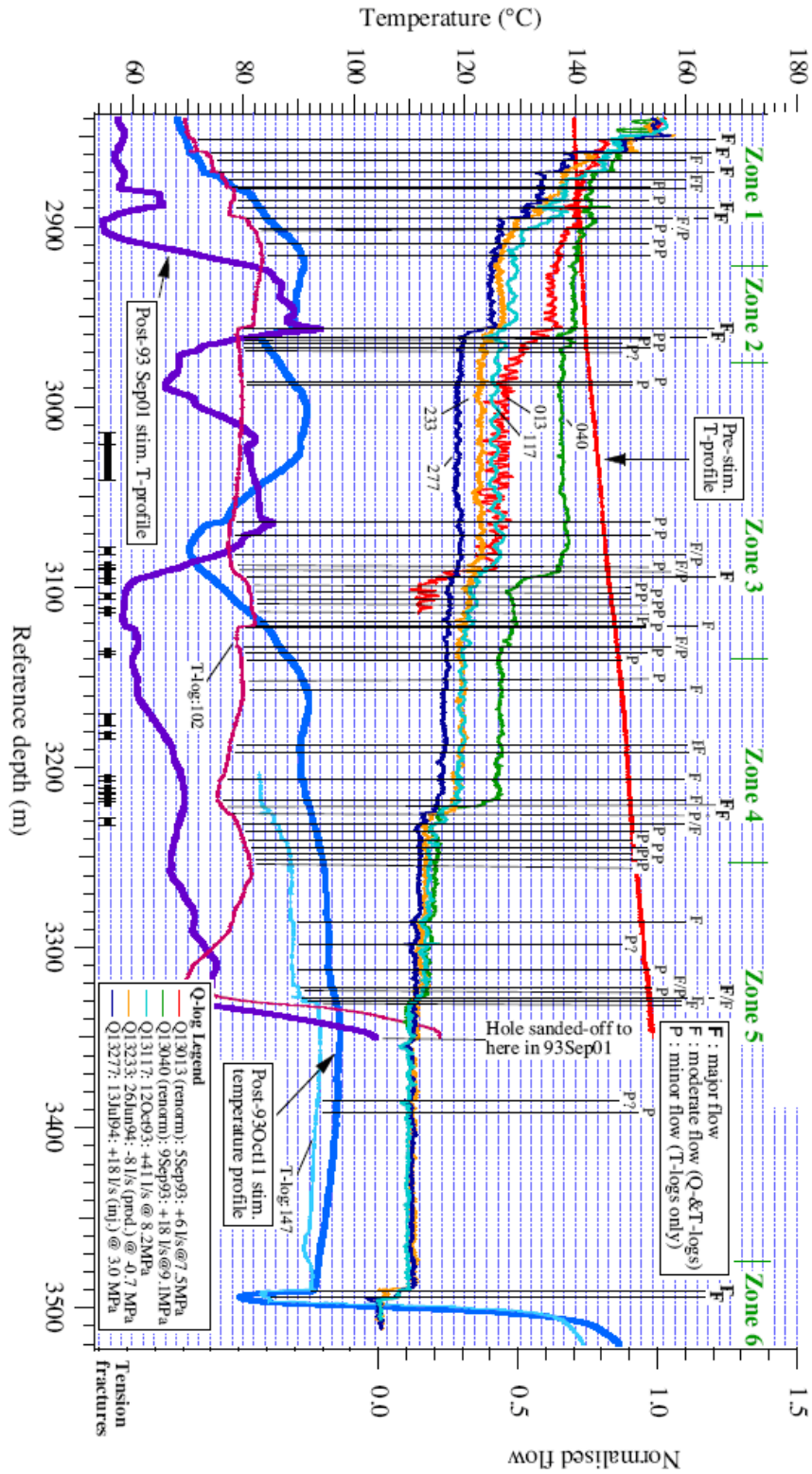


Figure 2-11: Flow and temperature logs from GPK1 post-stimulation. Permeable fractures are shown. Reproduced from Bachler et al. (2000).

Following hydraulic stimulation of the wells, flow logs allowed for a comparison between observed aperture and resulting, post-stimulation conductivity. One example is shown in Figure 2-12 (Henriksen, 2001). The chart plots the fractures in GPK1, a Soultz well that was drilled to 3.5km and stimulated. The figure shows the depth of each observed fracture and the fracture aperture. Fractures that were conductive following hydraulic stimulation are labeled P, F-min, or F-maj, listed in increasing order of conductivity.

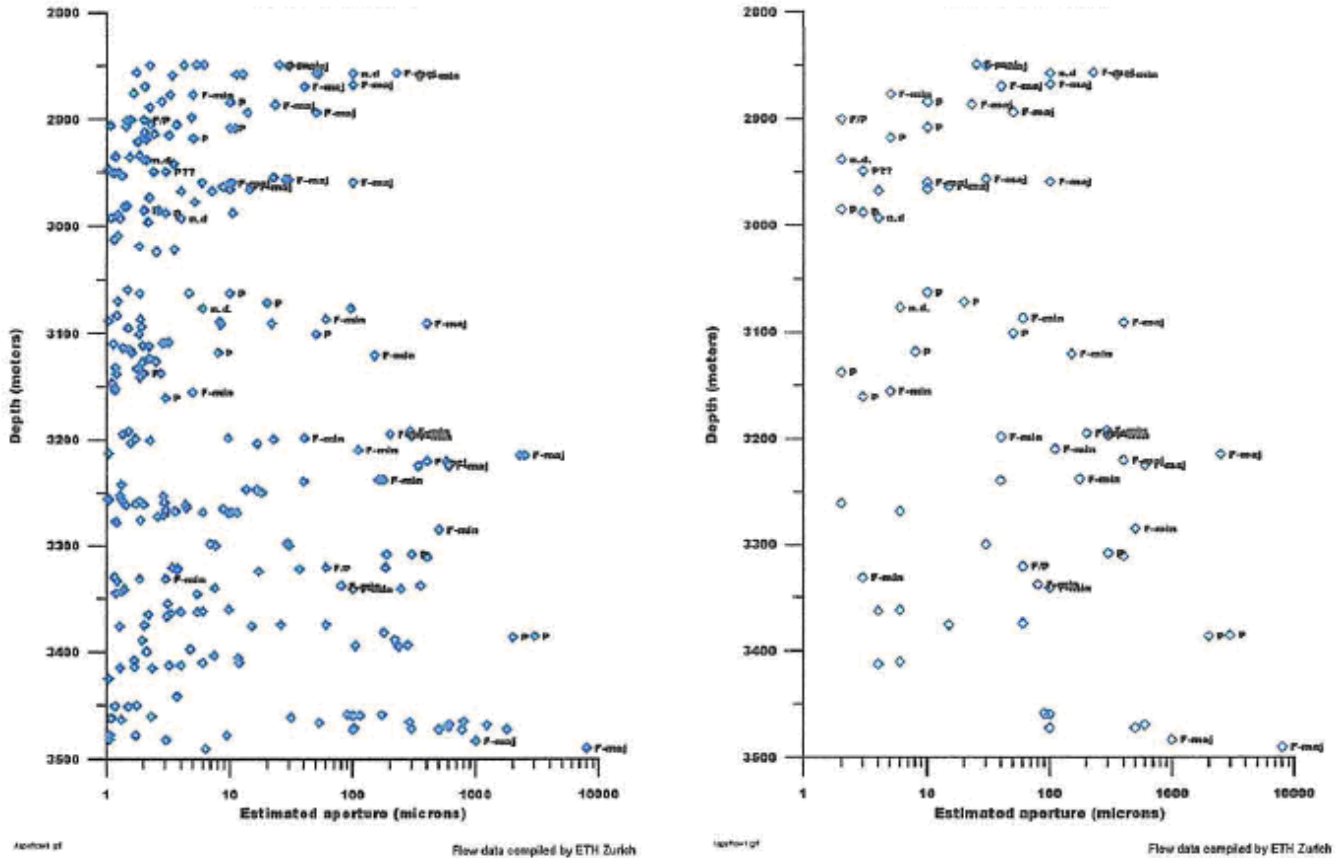


Figure 2-12: Reproduced from Henriksen (2001). Henriksen interpreted the aperture of the fractures and used qualitative flow data and temperature logs interpreted by Bachler et al. (2000).

Figure 2-12 demonstrates that there was a correlation between fracture aperture and the conductivity following stimulation. Figure 2-12 also demonstrates that many large aperture fractures were not stimulated at all. Even among the fractures that were stimulated, there was a large variation in conductivity. Evans et al. (2005a) noticed that stimulation tended to be more effective in regions of the borehole where the granite showed significant alteration.

It can be concluded that following stimulation of GPK1, a small number of discrete fracture zones controlled flow in and out of the wellbore. Wider aperture fractures, which were located in clusters of greater fracture density, tended to be conductive following stimulation. The correlation was weak, with some wide fractures not being well

stimulated and other small and moderate fractures being significantly stimulated. In the deeper Saultz wells, GPK2, GPK3, and GPK4, it was also observed that only a handful of fractures were significantly conductive following stimulation, (Baria et al., 2005 and Tischner, 2006). The most extreme example is GPK3, where 70% of flow occurs out a single fracture. This is shown in Figure 2-13.

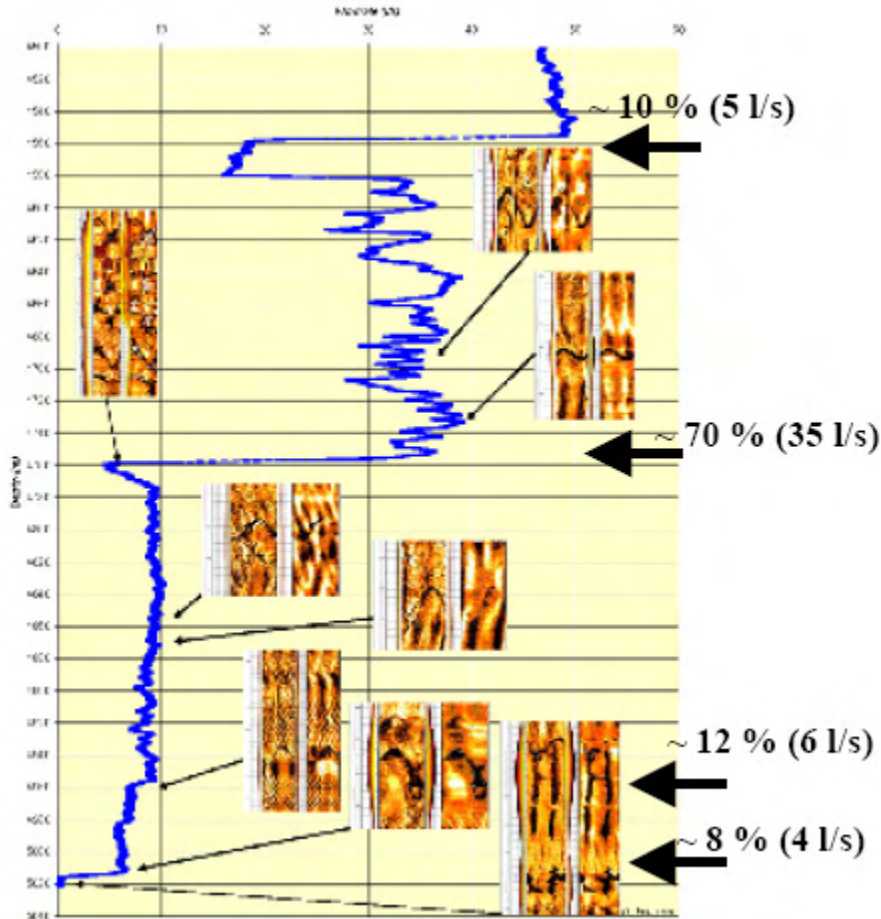


Figure 2-13: Flow log of GPK3 during hydraulic stimulation. Reproduced from Baria (2004).

Heterogeneity in stimulation effectiveness could represent an opportunity to improve the productivity of EGS wells. The fact that many large aperture fractures are not well stimulated suggests that if well conductivity could be improved if they were all stimulated. The fact that some smaller aperture fractures were well stimulated suggests that it is feasible to stimulate smaller fractures, which means that it may be possible to stimulate a far greater number of fractures than has been done in the past. Ideally a stimulation would improve conductivity in as many fractures as close to the wellbore as possible.

2.4.2. Critical Stress Analysis at Saultz

At Saultz, as described in Section 2.4.1, there was heterogeneity in the effect of hydraulic stimulation. A small number of fractures were stimulated significantly; a greater number

were stimulated mildly, and most were not stimulated. Given our understanding of the Coulomb failure criterion, orientation would be a likely candidate to explain variation in stimulation. Equations 2-10 and 2-11 indicate that the relative magnitudes of the shear and normal stresses depend on the orientation of the fracture plane. The effect of orientation can be studied using a technique called critical stress analysis. This technique has been successfully used in other geologic settings to predict which natural fractures intersecting a wellbore will be permeable. For examples, see Zoback (2007), Okabe and Hayashi (2000), and Ito and Zoback (2000). The premise is that fractures that are well oriented for shear according to the Coulomb failure criterion are likely to be mechanically active. Because shear enhances transmissibility, they are likely to be conductive. In this case stimulated transmissibility is being predicted instead of natural transmissibility. In principal the method should still apply.

Bachler et al. (2000) used critical stress analysis to analyze the effect of orientation on stimulation at Soultz. The results are summarized in Figure 2-14 and Figure 2-15. Bachler et al. used values of *in situ* stress state that were available from hydrofracture stress measurements, density logs, and focal mechanisms of microearthquakes caused by stimulation. The most recent estimates of *in situ* stress state were published by Valley and Evans (2007). The 2007 values are reasonably close to the values Bachler used in 2000.

Each dot on the Mohr diagram represents a different fracture, with the location of the dot in the chart being related to the orientation of the fracture. The lines represent the predicted frictional failure criterion. According to the theory, any dot located above the failure criterion line should correspond to a fracture which sheared. It is assumed the fractures do not have cohesion. The lines originating from the origin are the pre-stimulation failure criteria for various μ . The lines which are translated to the right are the failure criteria during stimulation, taking into account roughly 9 MPa of fluid overpressure which were applied during the stimulations.

Figure 2-14 and Figure 2-15 indicate that critical stress analysis was unsuccessful in predicting whether or not a fracture would shear. Being critically stressed was a necessary but not sufficient condition for stimulation. Permeable fractures poststimulation had a wide variety of orientations which were both favorable and unfavorable according to the theory. During the stimulation, virtually all the fractures lay above the failure criterion (for both choices of μ), but only a small fraction of them were actually stimulated.

Bachler et al. (2000) suggest three explanations. (1) The fractures have cohesion. (2) There is significant heterogeneity in stress state along the fracture which is not taken into account by their stress model. (3) Fractures were stabilized by poroelastic stress in the matrix surrounding them.

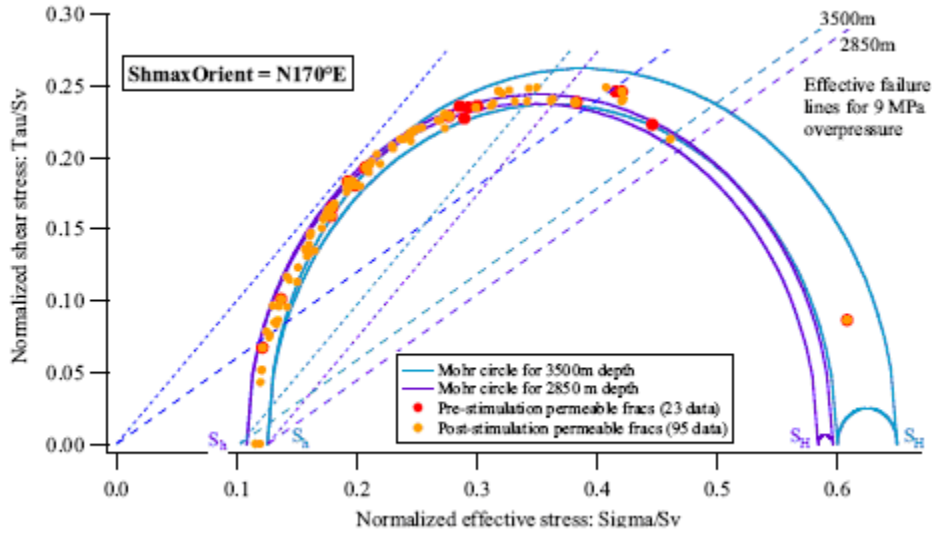


Figure 2-14: Mohr diagram with permeable fractures before and after stimulation of GPK1. Reproduced from Bachler et al. (2000).

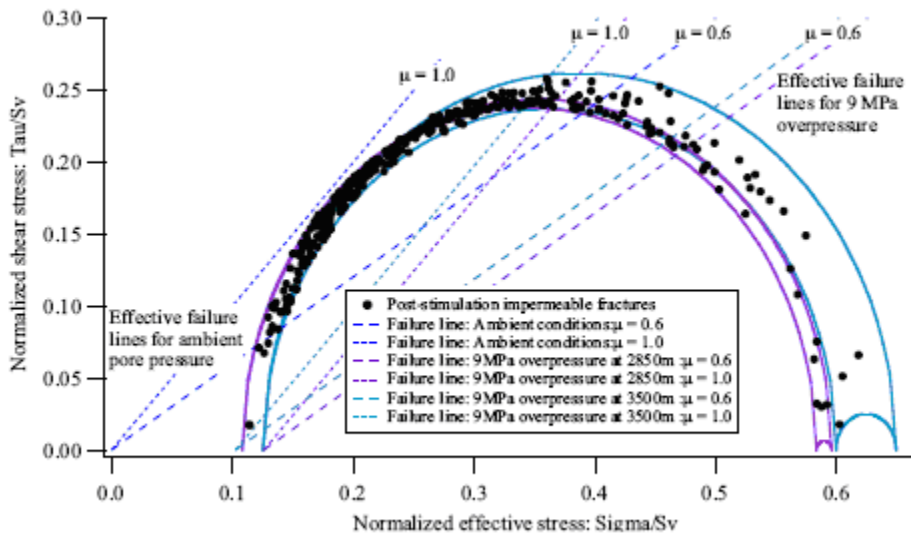


Figure 2-15: Mohr diagram of non-permeable fractures before and after stimulation of GPK1. Reproduced from Bachler et al. (2000).

Evans (2005b) addressed these conjectures and concluded that only fracture cohesion was capable of explaining the data. He concluded that fracture cohesion of at least 6MPa was needed to keep the majority of the fractures stable. Cohesion would have the effect of translating the failure line vertically. Evans noted that fractures in areas of significant alteration of the granite were more likely to be stimulated than fractures in unaltered granite. He suggested that difference in fracture infilling could account for the difference

in cohesion. This conjecture is consistent with the rock mechanics literature as discussed in Section 2.2

Another point that is illustrated in Figure 2-15 is that because of the trends in stress with depth, the shallower fractures are somewhat more favored to shear than the deeper fractures.

Another possible explanation has to do with the transmission of the injection pressure into the fractures. The diffusion of the pressure response in the fractures from the wellbore injection is governed by the diffusion equation, which assuming only radial flow and constant fluid properties is (Horne, 1995):

$$\frac{\partial^2 P}{\partial r^2} + \frac{1}{r} \frac{\partial P}{\partial r} = \frac{\phi \mu_l c_t}{k} \frac{\partial P}{\partial t} \quad (2-19)$$

where P = pressure, r = radius, ϕ = porosity, μ_l = viscosity, c_t = total compressibility, and k = permeability. There is no way of knowing what the permeability of the naturally sealed fractures. A small number appeared to take flow prior to stimulation. A lower bound on the permeability is not known, but many probably have exceptionally low permeability. The rate that the pressure increases in the fractures surrounding the wellbore during stimulation is related to the hydraulic diffusivity, $\frac{k}{\phi \mu_l c_t}$, or α . A tightly

sealed fracture with low hydraulic diffusivity would transmit the pressure signal very slowly. The result might be that over the time period of the stimulation, a few days at most, the pressure in the fracture is still much lower than the pressure of the fluid in the wellbore.

Note that here, the term permeability is used to refer to fractures, where in other places in the report the term transmissibility is used. Flow rate is proportional to permeability times thickness. Transmissibility lumps permeability and thickness into a single number. Because fracture thickness may not be known, transmissibility is usually the most appropriate term to use when referring to a fracture. In this section of the report, only radial flow is considered and the absolute magnitude of flow rate is irrelevant. For this problem, “thickness” is not relevant. Therefore, in this section, permeability is used.

There is not an analytical solution for Equation 2-19 (Ehlig-Economides, 1979). There is an analytical solution for the one-dimensional diffusion equation:

$$\frac{k}{\phi \mu c_t} \frac{\partial^2 P}{\partial x^2} = \alpha \frac{\partial^2 P}{\partial x^2} = \frac{\partial P}{\partial t} \quad (2-20)$$

Assuming constant pressure injection, the solution is (Bird, Stewart and Lightfoot 2007):

$$\frac{P - P_{init}}{P_b} = 1 - erf\left(\frac{x}{\sqrt{4\alpha t}}\right) \quad (2-21)$$

This solution is instructive to show that the penetration depth scales like the square root of time. This behavior is seen in all diffusive processes. However, the assumption of one-dimensional flow is a very gross approximation. It would be more useful to solve the diffusion equation for radial flow. A solution exists for Equation 2-19 when it is transformed to Laplace space. There is not an analytical inversion, but the solution can be inverted numerically using an inverse Laplace transform algorithm.

First define the dimensionless variables:

$$r_D = r / r_w \quad (2-22)$$

$$t_D = \frac{kt}{\phi\mu_i c_t r_w^2} \quad (2-23)$$

$$P_D = \frac{P_{init} - P}{P_{init} - P_{inj}} \quad (2-24)$$

Where r_D is dimensionless radius, t_D is dimensionless time, P_D is dimensionless pressure, and r_w is the radius of the well.

The boundary conditions are chosen to be constant pressure injection and with an infinite outer boundary. Infinite outer boundary is an appropriate boundary condition if the pressure signal has not propagated far enough into the fracture to reach the outer part of the fracture. Because in this case the behavior of very low permeability fractures is primarily being considered, it is reasonable to assume the pressure signal will not travel very far and is unlikely to be affected by the fracture edge.

During many stimulations at Soultz, the injection pressure was constant even as flow rate was held constant. That is unusual behavior for injection into a well and occurs because the stimulation increases both the conductivity and pore volume of the fractures. For a low permeability, unstimulated fracture, the effect of stimulation is not significant. An unstimulated fracture is affected only by the constant pressure in the wellbore. During constant pressure injection, injection rate declines with time. Even though this is not what happened in the well overall, this is what would happen in an isolated, unstimulated fracture.

The solution to the radial diffusivity equation in Laplace space for constant pressure injection and infinite outer boundary is (Ehlig-Economides 1979):

$$\bar{P}_D = \frac{K_0(r_D \sqrt{s})}{sK_0(\sqrt{s})} \quad (2-25)$$

Where \bar{P}_D is Laplace space dimensionless pressure, s is the Laplace variable, and K_0 is the modified Bessel function of the second kind of zeroth order.

Equation 2-25 can be inverted back to time space using an inverse Laplace transform algorithm. The Gaver-Stehfest algorithm was used. A freeware Matlab code was downloaded to implement the algorithm (Srigutomo, 2006).

To make the results tangible, reasonable values were chosen for the variables. The values were: $\mu_l = 10^{-4}$ Pa-sec., $c_l = 4 \times 10^{-10}$ Pa $^{-1}$, $\phi = 0.01$, $r_w = .25$ m, $P_{init} = 40$ MPa, and $P_{inj} = 55$ MPa. These are rough estimates for the conditions at 4500m during the stimulations of the deeper wells at Soultz.

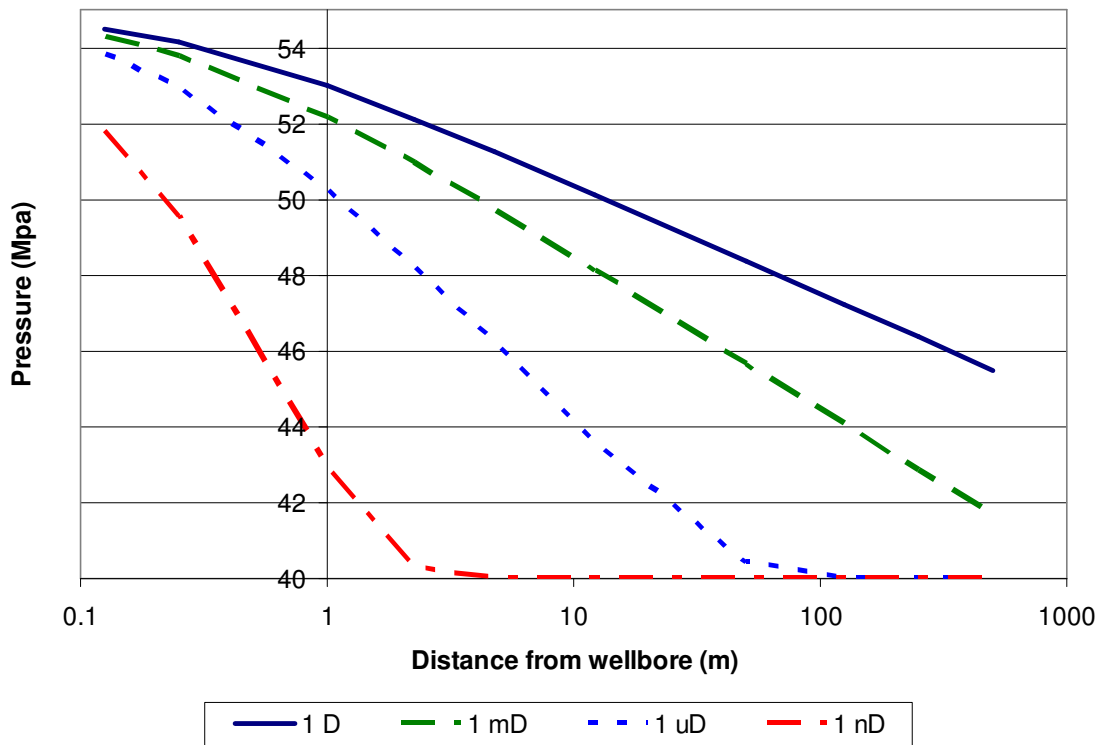


Figure 2-16: Radial pressure distribution in an isolated, infinite fracture after three days of constant pressure injection for different values of permeability.

There are no data on the permeability of the tightly sealed fractures at Soultz. It would be reasonable to assume their permeability is on the order of microdarcies to nanodarcies. For such a low permeability fracture, Figure 2-16 shows that the pressure would be significantly below the injection pressure only a few meters away from the wellbore. Interestingly, even for the modest permeability 1 md fracture, the pressure is 5 MPa below the injection pressure about 5 m away from the wellbore.

It is not clear how much of the fracture needs to experience elevated pressure in order to fail in shear. It may be that only a tiny bit of the fracture needs to experience pressure

exceeding the Coulomb failure criterion. If so, it is unclear if shear failure would be isolated to that bit of the fracture or if failure on the small patch would cause a chain reaction and the entire fracture would slip. If a larger area of the fracture needs to exceed the failure criterion for slip to occur, it may be that a few days of stimulation isn't enough time to build up pressure and cause failure in a very low permeability fracture.

2.4.3. A Simple Model of the Effect of Heterogeneity

Stimulation heterogeneity is worth close examination. Consider the following line of reasoning: a well intersects 200 fractures that are optimally oriented for shear failure, but ten have an especially low coefficient of friction. Those ten would shear first and would intersect many more fractures. It is likely some of the newly intersected fractures would have a low coefficient of friction, and they would shear next. As this process continues, more fractures would become hydraulically connected to the wellbore and odds are that some of them would have especially low friction. For this reason it would become increasingly unlikely that one of the original critically-oriented, unstimulated fractures intersecting the wellbore would ever shear. The wellbore pressure would remain relatively constant over the length of the stimulation as long as the pressure drop in the stimulated fracture network is low because the shearing fractures would have increased pore volume. This process would tend to create a reservoir that rapidly grows away from the wellbore, but is poorly connected and has bottlenecks to flow. The overall conductivity of the reservoir would be higher if all well oriented fractures sheared, creating a more uniform, well-connected network.

To illustrate the potential effect of order and friction heterogeneity on reservoir properties, a simple model of stimulation was developed. The model grossly oversimplifies the system. It is intended only to investigate the potential impact of stimulation heterogeneity. The model stochastically generates a two-dimensional fracture set with an exponential size distribution and two possible orientations. Then the model sequentially "shears" fractures in the reservoir. Only fractures touching the wellbore or a previously sheared fracture are eligible to be sheared. The wellbore is shown in green. Stimulated fractures are blue, and unstimulated fractures are red.

In Figure 2-17, the algorithm stimulated eligible fractures randomly. In Figure 2-18, each fracture had a constant "propensity to fracture." At each step, the eligible fracture with the highest propensity was sheared. The stimulation in Figure 2-17 grew out slowly, forming a dense, well-connected fracture network around the well. The stimulation in Figure 2-18 grew farther afield, randomly, and with significant bottlenecking of flow.

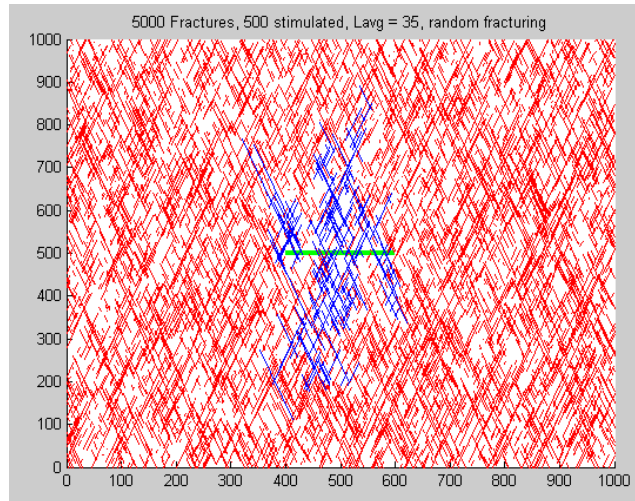


Figure 2-17: Random fracturing

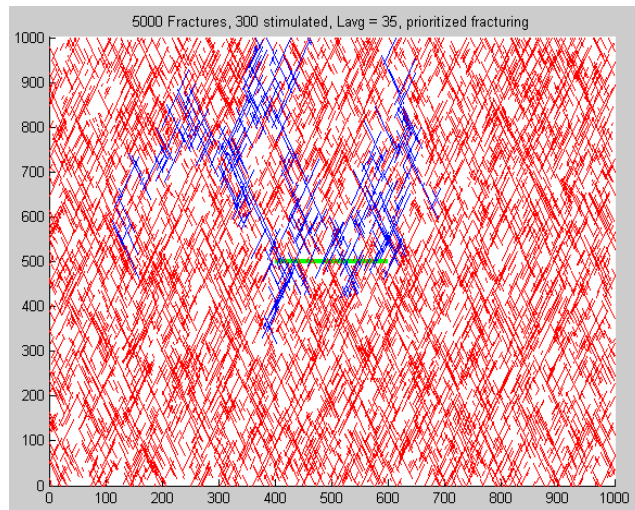


Figure 2-18: Prioritized fracturing

A Matlab (Mathworks, 2007) code was written that discretizes two-dimensional fracture networks to a connection list for simulation. The code writes a TOUGH2 input file, runs the simulation in TOUGH2, reads the output file, and plots the results. TOUGH2 is a multipurpose reservoir simulator developed at Lawrence Berkeley National Laboratory (Pruess et al., 1999). The Matlab code stochastically generates the fracture network. The discretization is performed by a two-dimensional mesh generator called Triangle (Shewchuck, 1996). The triangular matrix elements are thrown away and only the fracture elements are included in the simulation. In order to handle aspects of transmissibility calculations between fractures located at intersections, a code called “otpfabeta.exe” was used. The code was written by Mohammed Karimi-Fard (karimi@stanford.edu), a researcher at Stanford University (Karimi-Fard et al., 2004).

Stimulation with variable propensities to shear (like Figure 2-18) was simulated and then flow simulation was performed between two arbitrary locations in the reservoir. The result is shown in Figure 2-19. Red fractures support a high flow rate, blue fractures support a low flow rate, and purple fractures are somewhere in between. It is apparent that the flow channels through a very narrow path and that only a small percentage of the total stimulated volume is accessed by the flow.

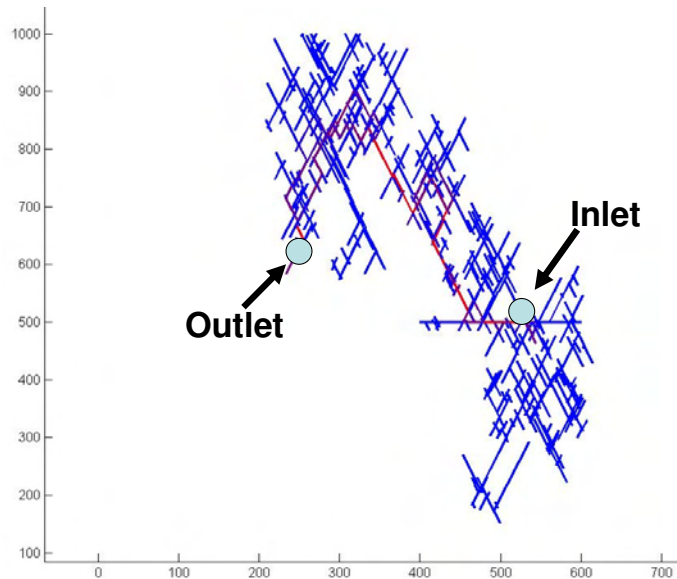


Figure 2-19: Flow rate through a “prioritized fracturing” model.

This exercise is not intended to be a rigorous model of fracture stimulation. However, it illustrates the point that heterogeneous stimulation could have profoundly negative implications on the structure of an EGS reservoir.

Chapter 3

3. Stimulation Modeling

3.1. Effective Continuum vs. Discrete Fracture Modeling

The next step is to develop a more sophisticated model of EGS reservoir stimulation. Such a model would have to be able to handle the coupled fluid flow, heat flow, thermoelasticity, and elastic and inelastic deformation.

Most reservoir modeling uses effective continuum modeling (ECM). These models use large, typically rectangular, grid blocks. Within each grid block, properties such as pressure and temperature are constant. If the reservoir is fractured, a dual porosity model is used. A dual porosity model assumes a given geometric shape to the fractures, usually evenly shaped orthogonal fractures. The properties of all the fractures in a grid block are assumed to be homogenous, as are the properties of the non-fractured rock. The interaction between the fractures and matrix is calculated using a function that is derived from assumptions about the shape of the fracture system.

Effective continuum models have significant limitations for modeling EGS stimulation. Fractures have very heterogeneous properties of transmissibility, aperture, orientation, and propensity to be stimulated. Some of these properties change significantly during the period of the modeling, in a way that is dependent on the individual fracture. The geometric relationship of the fractures is crucial. For example if two major pathways are parallel, they could be close to one another and not hydraulically interact at all. A small number of discrete pathways control flow, making it impossible to average out the effect of the fractures in the grid blocks. Dual porosity is intended for systems with a large number of well connected fractures so that their properties can be easily averaged out over the size of a grid block.

Given a reasonable realization of the fracture network, sophisticated upscaling techniques exist to turn the fracture network into an effective continuum model that matches pressure and tracer results. But there are no existing techniques that upscale heterogeneity in fracture stimulation behavior. Worse, the geometry of the fracture network is exactly what is not known and needs to be discovered through modeling! Hence effective continuum models lack predictive power in an EGS setting because they require assumptions about fracture spacing and geometry. The fracture spacing and geometry is exactly what EGS stimulation modeling intends to investigate. Even given assumptions of fracture geometry, it is a complex upscaling challenge to turn the fracture realization into an effective continuum model.

This paper proposes to use discrete fracture modeling (DFM) instead of effective continuum modeling. DFM directly models flow through a network of fractures. An example of a Discrete Fracture Network is shown in Figure 3-1. This would allow for direct consideration of the impact of fracture geometry on fluid flow and stimulation.

The biggest drawback to DFM is that it is very difficult to discretize in three dimensions. Fractures form complex interlocking shapes and creating volume elements that fill the space between the fractures is a tremendous challenge. In the case of EGS stimulation, it is not necessary to discretize the volume. Because flow only occurs through the fractures, the matrix can be disregarded. Heat flow in the volume can be accurately accounted for with a one-dimensional approximation on a time scale of days, the maximum duration of EGS stimulation, because the penetration depth of conduction would only be a few meters. Stress interaction between the fractures has not been accounted for in previous EGS modeling work. This paper will lay out how to use the boundary element method (BEM) to model stress interaction. BEM does not require discretization of the volume, only the fractures. In the case of a fracture held in place by friction, thermoelastic effects can be calculated knowing only the temperature at the fracture as long as fracture thermal interaction is negligible.

This chapter lays out a design for a simulator tailored for EGS stimulation. First, previous EGS modeling work using DFM will be summarized. FracMan, a DFM package from Golder Associates will be mentioned briefly as a useful and readily available tool for DFM. Methods for generating a geologically realistic realization of a fracture network are discussed. Then the mathematical treatment of fluid flow, heat flow, stress, thermoelasticity, and frictional shear will be laid out. In future work these will be integrated into a simulation program in C++.

3.2. Previous Work

Discrete fracture modeling has been applied to EGS for over 15 years. Earlier models were developed for different purposes and have relative strengths and weaknesses. Examples are FRACTure (Kohl and Hopkirk, 1995), GEOTH3D (Yamamoto et al., 1997), FRACSIM-2D (Willis-Richards et al., 1996), FRACSIM-3D (Hossain, 2002), Geocrack2D (Swenson and Hardeman, 1997), HEX-S (Kohl et al., 2005), FRACAS (Bruehl et al., 2002), GMRS (Yoshioka et al., 2008) and an untitled model by Rahman et al. (2002). Commercially available packages that have been applied to EGS modeling are gOcad and FracaFlow (Sausse et al., 2008) and Petrel (Schlumberger) (Kovac et al., 2009).

Some EGS models assume the geometry of the stimulated reservoir *a priori*. Other EGS models assume the geometry of the unstimulated reservoir and attempt to model the stimulation process. Geologic data are integrated using geostatistics to construct a pre-stimulation discrete fracture model. Then coupled hydrogeomechanical modeling describes how the stimulation causes shear and other effects on fracture in the formation and forms the reservoir. The result is either a discrete fracture model or an effective

continuum model for flow simulation. Notable examples of this approach are the models of Jing, Rahman, Kohl, and Bruel. Yoshioka et al. modeled the propagation of a single planar tensile fracture.

This research envisions improving on previous models in a number of respects. (1) Boundary element method will be used to model the interaction of fractures as they shear. (2) Novel methods of building a geologically realistic discrete fracture model will be investigated. (3) The impact of heterogeneity in frictional strength will be investigated. (4) Optimization of both EGS stimulation and wellbore design will be studied.

3.3. DFN Static Model

3.3.1. Golder FracMan

Golder FracMan is a commercial software package that can be used to generate a discrete fracture model. FracMan can generate fractures stochastically and discretize them. The output can be exported to text format. The format is a list of nodes and their locations and a list of elements and which nodes are in each element. FracMan can also import a DFN with various element properties such as pressure or temperature. This feature could be used to visualize the results of simulation. It would also be possible to use some other program to generate the fracture network and perform the discretization in FracMan.

FracMan has many features that facilitate the generation of a DFN. The fracture density can be uniform or spatially variable. Fractures can be conditioned to a well log, so that the fractures intersecting a well in the DFN are the same as observed in the log. Fracture properties are chosen according to a given statistical distribution. Properties can be correlated. For example, fracture radius could be correlated to aperture. Multiple fracture sets can be defined, and truncation rules can be defined to specify the percentage of fractures that truncate against each other and those that pass through.

A screen shot of a typical FracMan DFN is shown in Figure 3-1.

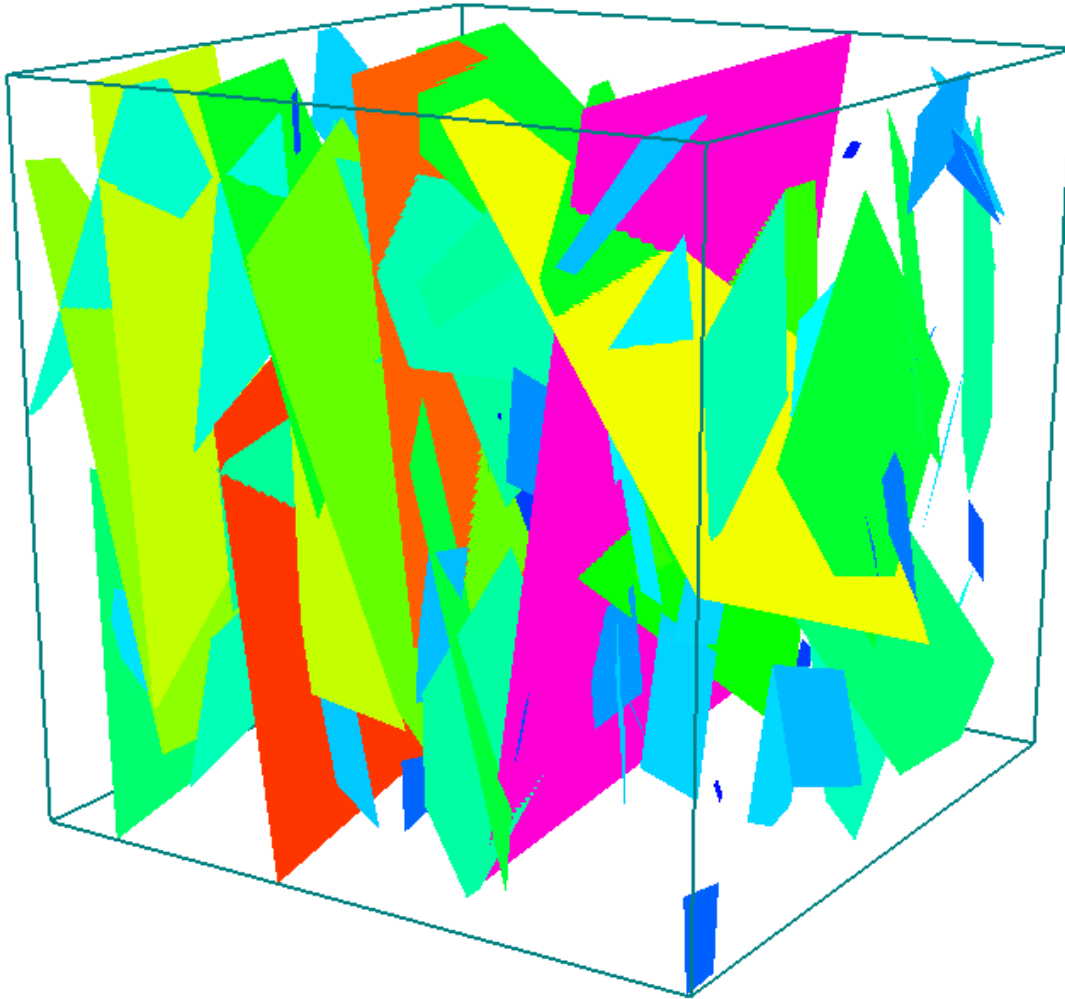


Figure 3-1: DFN Generated in FracMan.

In conclusion, FracMan is a valuable tool for DFN modeling that can be used in conjunction with the stimulation simulator envisaged in this report for generation and discretization of a DFN and visualizing the results of simulation.

3.3.2. Static Model Generation

There are significant limitations to gathering of data to constrain the geometry of the preexisting fracture network.

Commonly, seismic data are used in oil and gas to visualize fractures in rock. Unfortunately seismic surveys do not work well in crystalline rock. Seismic reflections occur at interfaces between rocks with different properties. Such interfaces are common in sedimentary rock which consists of different layers. Crystalline rock is relatively homogenous.

Some studies have attempted to use seismic analysis to identify major fractures in an EGS reservoir (Bachler et al., 2000). Presumably the alteration in the fracture itself was enough to create a reflector. This method was implemented by locating seismic receivers in the borehole and setting off explosive charge down hole. This method appeared to have been able to identify a handful of large faults.

Microseismic events during stimulation can be located in the rock, which gives an idea of where the stimulation is occurring. At its best, microseismic analysis appears capable of visualizing major hydraulic features in the rock (Evans et al., 2005c). A drawback to microseismic analysis is that it does not give any information about fractures in the rock that are not stimulated.

The only way to observe fractures in the rock directly is by using wellbore image logs, which can actually visualize the fractures as they cross the wellbore. The challenge is how to infer three-dimensional properties of fractures from one-dimensional well images. For example FMI logs give the aperture and orientation of fractures intersecting the wellbore but do not measure spatial extent. Wu and Pollard (2002) suggested techniques for extrapolating the 3D geometry of the fractures from the wellbore.

Fracture spacing is an important issue. Fracture spacing is often regular in many sedimentary outcrops, but this is caused by mechanical bedding layers. In crystalline outcrops, it is observed that fractures cluster. Fractures do not appear to be randomly located in space. The well logs at Soultz indicate that the fractures are clustered (Bachler et al., 2000). If so, then this spatial variability should be taken into account by the algorithm that locates the fractures in space.

Different approaches have been followed to handle fracture spacing in DFNs. One approach is to locate fractures randomly in space. This is the simplest, but unlikely to be realistic. It has been observed in many studies that fractures have fractal geometry. Algorithms can be used to generate fractally distributed fracture distributions. An application of this technique is described in Acuna and Yortsos (1995). FracMan will locate fractures randomly or according to a fractal process. FracMan also has a third algorithm, in which the user specifies a few major fractures deterministically and then the rest are located stochastically, with fracture density increasing with proximity to the major fractures (FracMan, 2009).

There are many other methods of building fracture networks. One approach is to define fracture densities on a regular grid, then populate fractures inside the reservoir based on the densities. This can be combined with geostatistical methods that are used to define fracture densities. These same methods are used to define fracture densities for effective continuum models.

Tamagawa and Pollard (2008) used knowledge of a few major faults to predict density of smaller faults. They solved a Displacement Discontinuity problem (described in Section

3.4.5) based on the geometry of the major faults and calculated the stress in the reservoir. Based on the stress, they identified where stress should be conducive to fracturing.

Tamagawa et al. (2002) used Sequential Indicator Simulation, a common geostatistical technique (Goovaerts, 1997), to define a distribution of fracture density on a grid. Other statistical techniques, such as a neural network, could be used to predict fracture density. An example is El Ouahed et al. (2003). These techniques are common practice in effective continuum modeling.

A drawback to these methods is that realizations usually do not look “geological.” A simple visual comparison of the DFN with an actual rock outcrop indicates they appear different. It is not clear whether or not it is necessary to generate a “realistic looking” DFN in order to model fluid flow accurately. There are some algorithms that have succeeded at producing realistic looking DFNs.

One strategy is to “grow” fractures in an attempt to mimic the process by which they formed. This technique is capable of generating DFNs that appear geologically realistic. Examples are Olson and Pollard (1990) and Renshaw and Pollard (1994). These studies seeded tiny tensile cracks randomly in a two-dimensional plane and allowed them to grow iteratively. The perturbation in stress caused by their opening and growth was modeled using the Displacement Discontinuity method. Based on the stress intensity at the fracture tips, fractures grew deterministically and formed patterns of clustering that were consistent with observations. Mutlu and Pollard (2008) allowed the fractures to fail in shear and modeled the formation of secondary tensile fracture of their tips. Bergbauer and Martel (1999) suggested that the orientation of joints formed by cooling of the pluton would be affected by the shape of the pluton.

Srivastava (2006) built a three-dimensional DFN based on a chalk quarry as part of work for Ontario Power Generation's Deep Geologic Repository Technology Program to investigate the safety of geologic storage of waste. Srivastava seeded fractures, but rather than solving the Displacement Discontinuity problem for their stress intensity factor, he used statistical methods to allow the fractures to grow stochastically. Srivastava was able to create a three-dimensional DFN network that appeared realistic compared to the fracture traces on the wall of the quarry. Another mixed stochastic/deterministic method is that of Hoffman et al. (2004).

Keeping in mind the geologic process of fault formation described in Section 2.3, it might be possible to use an approach similar to that of Olson and Pollard or Srivastava to model the formation of faults in granitic rock. This modeling could have application to the generation of DFN for modeling and also for describing fundamental aspects of the reservoir such as fault intersections.

By far the most common technique in DFM is to locate the fractures randomly in space. There is no theoretical reason to do this, but it is the simplest technique to apply. All of

the examples of DFM for EGS listed in Section 3.2 located the fractures randomly in space.

3.4. Hydro-Thermo-Mechanical DFN Simulation

3.4.1. Overall Modeling Strategy

The simulator needs to deal with (1) mass transport, (2) energy transport, (3) thermoelasticity, (4) Coulomb failure, and (5) stress interaction between fractures.

Heat and mass transfer between fracture elements can be handled using standard finite difference techniques. Heat conduction from the granite surrounding the fractures can be accurately handled with a one-dimensional conduction approximation on short time scales. Thermoelastic effects can be calculated knowing the temperature of the fractures. Fractures slip can be calculated using a Coulomb failure criterion algorithm. Stress interaction of slipping fractures can be modeled using the Displacement Discontinuity method, a type of Boundary Element Method.

The overall model algorithm is shown in Figure 3-2. For each time step, the mass and energy flow equations are solved for the pressure and temperature of each fracture element. These values are used to calculate the normal and shear traction on each element. The Coulomb failure criterion is applied with the Displacement Discontinuity method to determine which fractures slip, and the transmissibility is updated accordingly. Then the process is repeated.

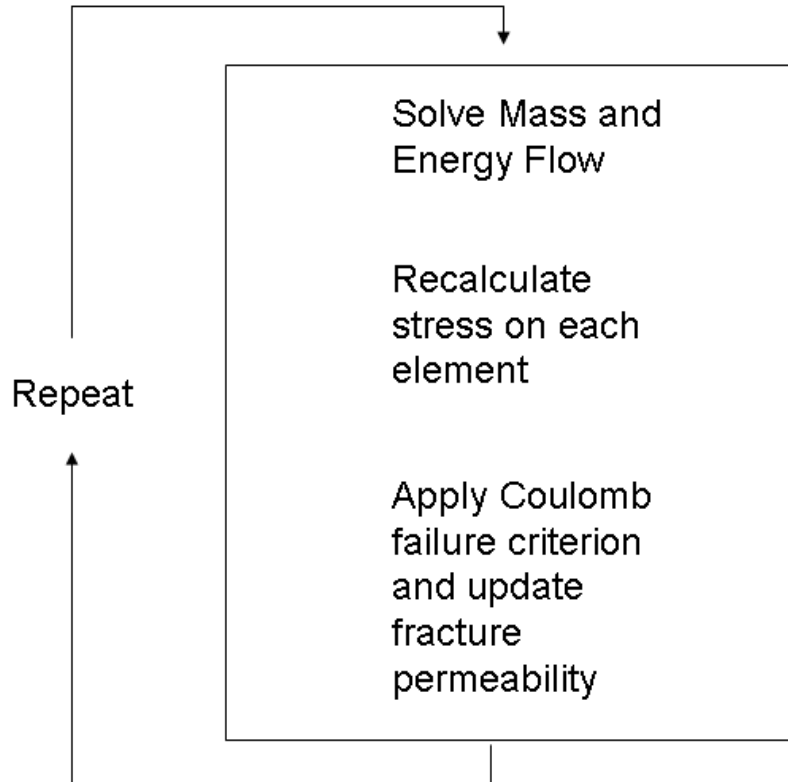


Figure 3-2: Overall modeling algorithm

3.4.2. Mass Balance

Fluid flow can be handled using a finite difference or finite element approach, which are standard in reservoir modeling. Most EGS reservoirs are deep enough that there is no steam present. If so, then a single-phase simulator is adequate. A good explanation of the mass and energy discretization for unstructured grids in flow simulation is in Pruess (1999).

The fractures are discretized into fracture elements. Each element m is connected to P elements between which flow occurs. M_m is the mass per bulk volume of the fluid in the element m . V_m is the volume of the element. F_{pm} is the mass flow rate between element p and m . q is a mass source term (typically a well) and t is time.

A mass balance on an individual fracture element gives:

$$\sum_{p=1}^P F_{pm} = V_m \frac{\partial M_m}{\partial t} + q_m \quad (3-1)$$

Darcy's law is:

$$\mathbf{u} = \frac{k}{\mu_l} (\nabla P - \gamma \mathcal{N}z) \quad (3-2)$$

where \mathbf{u} is the superficial velocity, distance per second, and γ is a gravitational constant. Discretization of Darcy's law gives the mass flow:

$$F_{pm} \approx u_{pm} A_{pm} \rho_{pm} = A_{pm} \left(\frac{k\rho}{\mu_l} \right)_{pm} \left(\frac{P_p - P_m}{D_{pm}} - \rho_{pm} g_{pm} \right) \quad (3-3)$$

where A_{pm} is the cross-sectional area between the two elements, g_{pm} is the component of gravitational acceleration between p and m , and D_{pm} is the sum of the distance from each element center to the interface between the elements. For a good discussion of the details of calculating geometrical values in discrete fracture models, see Karimi-Fard et al. (2004). For nonconstant variables, the nm subscript indicates that some kind of interpolation has been performed. Upstream interpolation would choose whichever value is in the cell where the flow is coming from. Other interpolations would average (arithmetic, harmonic, etc.) the values between the n and m element.

The mass per bulk volume in a cell m is:

$$M_m = \phi_m \rho_m \quad (3-4)$$

ρ is the fluid density and ϕ is porosity. The time derivative can be discretized to give:

$$\frac{\partial M}{\partial t} \approx \frac{M_m^{n+1} - M_m^n}{\Delta t} \quad (3-5)$$

where the superscript $n+1$ indicates the time step that is being calculated and the superscript n indicates the time step that was just calculated. The result is the equation:

$$\sum_{p=1}^p A_{pm} \left(\frac{k\rho}{\mu_l} \right)_{pm} \left(\frac{P_p - P_m}{D_{pm}} - \rho_{pm} g_{pm} \right) = V_m \frac{M_m^{n+1} - M_m^n}{\Delta t} + q_m \quad (3-6)$$

To solve the problem fully implicitly, all variable properties such as viscosity and density are evaluated at the future time step. Implicit evaluation is more computationally intensive, but gives much better stability. Permeability will be calculated explicitly (using the value from the previous time step), because the change in permeability depends on the complex Coulomb failure that will have to be evaluated between time steps. The result is:

$$\sum_{p=1}^P A_{pm} \left(\frac{\rho}{\mu_l} \right)_{pm}^{n+1} k_{pm}^n \left(\frac{P_p^{n+1} - P_p^n}{D_{pm}} - \rho_{pm}^{n+1} g_{pm} \right) = V_m \frac{M_m^{n+1} - M_m^n}{\Delta t} + q_m^{n+1} \quad (3-7)$$

Equation 3-7 is nonlinear and can be solved by using any nonlinear solver. Equation 3-7 must be solved simultaneously for all the elements in the problem, which creates a system of nonlinear equations. Most nonlinear solvers require evaluation of a gradient or Jacobian. These terms can be extremely lengthy but computation can be greatly aided by analytical math programs such as Wolfram's Mathematica. The mass balance equations must be solved simultaneously with the energy balance equations, which are described in the following section. Fluid properties and their derivatives are supplied by an equation of state.

3.4.3. Energy Balance

Heat flows by radiation, convection and conduction. Radiation can be neglected in this problem. Convection is heat flow driven by flow. An energy balance on the element m gives:

$$\sum_{p=1}^P (Cd_{pm} + Cv_{pm}) = V_m \frac{\partial E_m}{\partial t} + e_m \quad (3-8)$$

where Cd_{pm} is the conduction between elements, Cv_{pm} is the convection between elements, e is the energy source term, V_m is the volume of the element and E is the enthalpy density of the fluid in the element. The cross-sectional area between adjacent fracture elements is very small because they are very thin, so conduction between them can be neglected. Conduction between the fracture elements and the volume can be handled using Equation 3-50. There is no convection between the fracture and the volume because there is no flow in the volume. The energy balance becomes:

$$\sum_{p=1}^P F_{pm} E_{pm} + 2K \left(\frac{\theta_m^{n+1}}{d_m^{n+1}} - p_{c,m}^{n+1} \right) = V_m \frac{\partial E_m}{\partial t} + e_m \quad (3-9)$$

Where θ is temperature, p_c and d are given in Section 3.4.7, and K is the thermal conductivity. E_{pm} is upstream weighted so that it equals either E_p or E_m . The enthalpy of the flowing fluid is the enthalpy of the element from which it is flowing. Discretizing gives:

$$\sum_{p=1}^P F_{pm}^{n+1} E_{pm}^{n+1} + 2K \left(\frac{\theta_m^{n+1}}{d_m^{n+1}} - p_{c,m}^{n+1} \right) = V_m \frac{E_m^{n+1} - E_m^n}{\Delta t} + e_m^{n+1} \quad (3-10)$$

Enthalpy E is a function of temperature and pressure (dependence on pressure is weak) and can be taken from an equation of state.

To handle the mass flux terms F , there are two choices. The first is to solve the energy and mass equations together. In this case, there are two equations for each element. Equation 3-3 would be inserted into 3-10 and the system of equations assembled. A second choice is to decouple mass and energy transfer. The temperature dependent terms in the mass equations would be handled explicitly (using temperature from the previous time step). The mass transfer system would be solved and the mass flux between each element would be known. Then these values would be plugged into Equation 3-10 and the energy balance equations would be solved. Decoupling energy and mass transfer would decrease computational intensity significantly. It would be less accurate and less stable. Fluid properties such as density and viscosity change relatively slowly with changes in temperature for single phase liquid water, so decoupling might be viable.

3.4.4. *Boundary Element Method for Elastostatics*

The boundary element method is an approximate method of solution of partial differential equations. BEM transforms the problem to the boundary, so that the domain of the problem does not have to be discretized. This significantly reduces the number of elements and avoids the difficulty of domain discretization. This section explains the boundary element formulation for elastostatic fracture problems. A type of BEM called the Displacement Discontinuity method will be used to describe the perturbation of stress caused when fractures slip.

A good reference book on basic stress and elasticity is Jaeger et al. (2007). This section is primarily based on the Aliabadi (2002). An excellent treatment of two-dimensional elastostatics BEM and the Displacement Discontinuity method is Crouch and Starfield (1983). A good general introduction to BEM is Brebbia and Dominguez (1992). A specialized text for thermoelastic fracture mechanics is dell'Erba (2002).

The elastostatics problem solves for the stresses and displacements resulting from a specified boundary condition along the boundary. The problem can be solved within a closed volume or outside the volume in the infinite domain. The boundary could be arbitrarily shaped, so it is discretized into a series of elements. When both the traction and the displacement at every element is known, the problem is solved. In order to solve the problem, either the traction or the displacement must be defined at every boundary element. A simple example of discretization is shown in Figure 3-3. Decreasing the size of the elements improves the accuracy of the solution.



Figure 3-3: Discretization in BEM.

In this section and following sections, Einstein notation will be used to keep equations a manageable size. Appendix A explain Einstein notation.

The stress equilibrium equations are:

$$\frac{\partial \sigma_{11}}{\partial x_1} + \frac{\partial \sigma_{12}}{\partial x_2} + \frac{\partial \sigma_{13}}{\partial x_3} + b_1 = 0 \quad (3-11)$$

$$\frac{\partial \sigma_{21}}{\partial x_1} + \frac{\partial \sigma_{22}}{\partial x_2} + \frac{\partial \sigma_{23}}{\partial x_3} + b_2 = 0$$

$$\frac{\partial \sigma_{31}}{\partial x_1} + \frac{\partial \sigma_{32}}{\partial x_2} + \frac{\partial \sigma_{33}}{\partial x_3} + b_3 = 0$$

Where b_i is a body force. Written in the more compact Einstein notation, these relations are:

$$\sigma_{ij,j} + b_i = 0$$

In Einstein notation, Hooke's law is:

$$\sigma_{ij} = \lambda \delta_{ij} \epsilon_{kk} + 2\mu_m \epsilon_{ij} \quad (3-12)$$

where λ is the Lamé constant, and μ_m is the shear modulus of elasticity. ϵ is strain. For clarity, some of these equations are written in full:

$$\sigma_{11} = \lambda(\epsilon_{11} + \epsilon_{22} + \epsilon_{33}) + 2\mu_m \epsilon_{11} \quad (3-13)$$

$$\sigma_{12} = 2\mu_m \epsilon_{12} \quad (3-14)$$

Multiplying the stress equilibrium equations by an arbitrary function u_i^* and taking the volume integral over the infinite domain gives:

$$\int_V (\sigma_{ij,j} + b_i) u_i^* dV = 0 \quad (3-15)$$

Manipulation of this equation and application of stress-strain relations and the divergence theorem allows for derivation of Betti's reciprocal work theorem, which states:

$$\int_S t_i u_i^* dS + \int_V b_i u_i^* dV = \int_S t_i^* u_i dS + \int_V b u_i^* dV \quad (3-16)$$

Where t_i represents tractions on the boundary and u_i represents displacements either in the boundary or in the domain. Betti's theorem is a relation that holds between the solutions

to two boundary value problems with different initial conditions, primed and unprimed, using the same shaped boundary.

Next the primed values are taken to be the point source solutions. The point force solution u_i^* gives the vector displacement field at a point \mathbf{X} caused by a point displacement at a point \mathbf{X}' in the i direction. These solutions are referred to as Kelvin's solutions. In Einstein notation this is written:

$$u_i^* = U_{ij}(\mathbf{X}', \mathbf{X})e_j \quad (3-17)$$

Similarly,

$$t_i^* = T_{ij}(\mathbf{X}', \mathbf{X})e_j \quad (3-18)$$

U_{ij} is the effect on a displacement in the i direction at point \mathbf{X} because of displacement in the j direction at point \mathbf{X}' . The body force b_i is taken to be the Dirac delta function such that it has the property:

$$\int_V g(\mathbf{X})\Delta(\mathbf{X} - \mathbf{X}')dV = g(\mathbf{X}') \quad (3-19)$$

This relation holds true because the integral of the Dirac function is zero everywhere except at the point \mathbf{X}' , where it is one. Substituting these relations into Betti's reciprocal theorem gives Somigliana's identity for displacement, which is the starting point for BEM in elasticity theory:

$$u_i(\mathbf{X}') = \int_S U_{ij}(\mathbf{X}', \mathbf{x})t_j(\mathbf{x})dS - \int_S T_{ij}(\mathbf{X}', \mathbf{x})u_j(\mathbf{x})dS + \int_V U_{ij}(\mathbf{X}', \mathbf{X})b_j(\mathbf{X})dV \quad (3-20)$$

For clarity, this is written in full for the two-dimensional case:

$$\begin{bmatrix} u_1 \\ u_2 \end{bmatrix} = \int_S \begin{bmatrix} U_{11} & U_{12} \\ U_{21} & U_{22} \end{bmatrix} \begin{bmatrix} t_1 \\ t_2 \end{bmatrix} dS - \int_S \begin{bmatrix} T_{11} & T_{12} \\ T_{21} & T_{22} \end{bmatrix} \begin{bmatrix} u_1 \\ u_2 \end{bmatrix} dS + \int_V \begin{bmatrix} U_{11} & U_{12} \\ U_{21} & U_{22} \end{bmatrix} \begin{bmatrix} b_1 \\ b_2 \end{bmatrix} dV \quad (3-21)$$

Applying Hooke's law to Somigliana's identity for displacement gives Somigliana's identity for stress:

$$\sigma_{ij}(\mathbf{X}') = \int_S M_{kij}(\mathbf{X}', \mathbf{x})t_k(\mathbf{x})dS - \int_S S_{kij}(\mathbf{X}', \mathbf{x})u_k(\mathbf{x})dS + \int_V M_{kij}(\mathbf{X}', \mathbf{X})b_k(\mathbf{x})dV \quad (3-22)$$

Where M_{kij} is the effect of the traction in the k direction at point \mathbf{X}' on the ij stress, and S_{kij} is the effect of displacement at point \mathbf{X}' in the k direction on the ij stress.

The values M_{kij} , S_{kij} , U_{ij} , and T_{ij} come from Kelvin's solution for a point force and are defined:

$$U_{ij}(\mathbf{x}', \mathbf{x}) = \frac{1}{16\pi\mu(1-\nu)r} ((3-4\nu)\delta_{ij} + r_{,i}r_{,j}) \quad (3-23)$$

$$T_{ij}(\mathbf{x}', \mathbf{x}) = \frac{-1}{8\pi(1-\nu)r^2} \left(\frac{\partial r}{\partial n} ((1-2\nu)\delta_{ij} + 3r_{,i}r_{,j} - (1-2\nu)(n_j r_{,i} - n_i r_{,j})) \right) \quad (3-24)$$

$$M_{kij} = \frac{1}{8\pi(1-\nu)r^2} ((1-2\nu)(\delta_{ik}r_{,j} + \delta_{jk}r_{,i} - \delta_{ij}r_{,k}) + 3r_{,i}r_{,j}r_{,k}) \quad (3-25)$$

$$S_{kij}(\mathbf{x}', \mathbf{x}) = \frac{\mu}{4\pi(1-\nu)r^3} \left(3 \frac{\partial r}{\partial n} ((1-2\nu)\delta_{ij}r_{,k} + \nu(\delta_{ik}r_{,j} + \delta_{jk}r_{,i})) - 5r_{,i}r_{,j}r_{,k} + 3\nu(n_i r_{,j}r_{,k} + n_j r_{,i}r_{,k}) + (1-2\nu)(3n_k r_{,i}r_{,j} + n_j \delta_{ik} + n_i \delta_{jk}) - (1-4\nu)n_k \delta_{ij} \right) \quad (3-26)$$

where ν is Poisson's ratio, and n_i are the components of the unit normal vector of the plane the traction is acting upon. r is the distance from point i to point j :

$$r = \sqrt{(x_1 - x_1')^2 + (x_2 - x_2')^2 + (x_3 - x_3')^2} \quad (3-27)$$

This expression can be differentiated to find the values of the partial derivative terms, such as $r_{,i}$. The normal derivative of the distance with respect to the normal \mathbf{n} is:

$$\frac{\partial r}{\partial \mathbf{n}} = r_{,i}n_i = \frac{\partial r}{\partial n_1}n_1 + \frac{\partial r}{\partial n_2}n_2 + \frac{\partial r}{\partial n_3}n_3 \quad (3-28)$$

If it assumed that there are no body forces, the volume integral goes to zero and the problem has been transformed such that it lies completely on the boundary. Next the boundary is discretized as a series of straight lines. On each of these lines, the traction and displacement can be assumed to be constant. More accurate formulations allow traction and displacement to vary linearly or quadratically along the element. So the traction and displacement values can be pulled out of the integral. Finally, the point u_i is taken to the boundary, which introduces a constant term, C_{ij} , which equals $0.5\delta_{ij}$ on a smooth element. Now Somigliana's identity becomes:

$$C_{ij}(\mathbf{x}')u_j(\mathbf{x}') + \sum_{n=1}^N u_j(\mathbf{x}) \int_S T_{ij}(\mathbf{x}', \mathbf{x}) dS = \sum_{n=1}^N t_j(\mathbf{x}) \int_S U_{ij}(\mathbf{x}', \mathbf{x}) dS \quad (3-29)$$

The functions T and U are known and are integrated numerically to give a constant interaction coefficient. Gaussian quadrature is a favored method of integration. This requires the evaluation of the function at a relatively small number of points (perhaps three, four, or seven) and the summing of these terms with certain weighting factors. The location of the points and the weighting factors are tabulated in Gaussian quadrature tables. For a triangular discretization, the location of the evaluations can be given in a local triangular coordinate system (Brebbia and Dominguez, 1992):

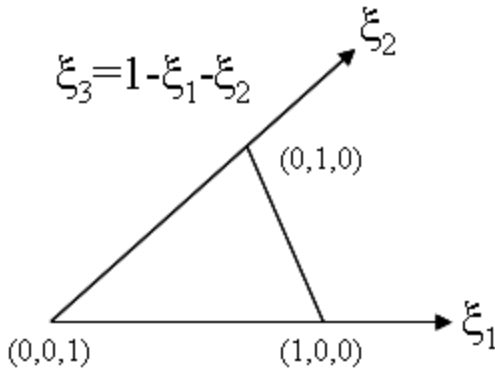


Figure 3-4: Triangular coordinate system.

The integral is evaluated numerically:

$$\int_0^1 \left(\int_0^{1-\xi_2} f(\xi_1, \xi_2, \xi_3) d\xi_1 \right) d\xi_2 = \sum_{i=1}^n g_i f(\xi_1^i, \xi_2^i, \xi_3^i) \quad (3-30)$$

where n is the number of integration points, and g_i is the weighting factor. For example, in the simple three-point integration, the function would be evaluated at the points corresponding to $(0.5,0.5,0)$, $(0,0.5,0.5)$ and $(0.5,0,0.5)$ in local coordinates and the weighting factor for all three points would be $1/6$. An even simpler approximation would be to evaluate the function at the element center and divide by two. The answer is then scaled according to the transformation back to the global coordinate system.

Once the interaction coefficients are calculated, the problem has been reduced to a system of linear equations. In order to fully specify the problem, either displacement or traction must be specified at each boundary point. Note that there are $3N$ values of displacement and $3N$ values of traction. With the constant interaction coefficients this is now a system of $3N$ linear equations. Combining all the terms together gives:

$$\mathbf{T}_b \mathbf{u}_b = \mathbf{U}_b \mathbf{t}_b \quad (3-31)$$

where \mathbf{T}_b and \mathbf{U}_b are the matrices of the interaction coefficients and \mathbf{u}_b and \mathbf{t}_b are the vectors of displacement and traction at each element. The subscript b is used only to differentiate these variables from other variables used in the report. The terms can be rearranged so that all the known values, either displacement or traction, can be moved to one side in a vector \mathbf{y} and the unknown placed in a vector \mathbf{x} with the corresponding interaction coefficients in a matrix \mathbf{A} . The result is a linear system of equations:

$$\mathbf{Ax} = \mathbf{y} \quad (3-32)$$

The system can be inverted to find the unknowns and the problem is solved. If desired, the displacements and stresses at interior points can be found by substituting back into Somigliana's identity. In this case, it is not necessary to solve a system of equations. Each interior point can be solved fully in terms of the boundary values.

The boundary element method creates a full matrix, with no zero values. The number of terms scales like the square of the number of elements, and so for large numbers of elements the method could be very memory and computationally intensive. The interaction terms such as U_{ij} do not change during the problem, so only need to be calculated once. As will be discussed later, in the application of this problem, not all the elements in the problem will be involved in the calculation, making the system much smaller.

3.4.5. *Displacement Discontinuity Method*

Fracture mechanics presents a unique difficulty for the BEM. In the case of a fracture, the "boundary" is the two opposing surfaces of the fracture which are located very close together or in the extreme case may be collocated. The two sides of the fracture can be expressed with (+) and (-) so that the displacement on one side is u_i^+ , and the other is u_i^- . It can be assumed that the displacement and the traction on opposing sides of the fracture are equal and opposite in sign. Then a variable can be introduced called the displacement discontinuity (Crouch and Starfield, 1983):

$$D_{in} = u_i^- - u_i^+ \quad (3-33)$$

In the three dimensions, the displacement discontinuity can be expressed as one normal displacement and two orthogonal shear displacements, acting on a plane with a normal \mathbf{n} .

In three dimensions, assuming that there are no body forces and that all the boundary conditions are specified as tractions, the displacement and stress due to the displacement discontinuity tensor are (Vandamme, 1989):

$$u_i(\mathbf{X}') = G_{ikn}(\mathbf{X}', \mathbf{x}) D_{kn}(\mathbf{x}) \quad (3-34)$$

$$\sigma_{ij}(\mathbf{X}') = H_{ijkn}(\mathbf{X}', \mathbf{x}) D_{kn}(\mathbf{x}) \quad (3-35)$$

The kernels G_{ijkn} and H_{ijkn} are defined:

$$G_{ijkn}(\mathbf{x}) = -\frac{1}{8\pi(1-\nu)} \left(\frac{1-2\nu}{r^3} (r_i \delta_{kn} - r_n \delta_{ki} - r_k \delta_{in}) - \frac{3r_i r_k r_n}{r^5} \right) \quad (3-36)$$

$$\begin{aligned} H_{ijkn}(\mathbf{x}) = & -\frac{\mu}{4\pi(1-\nu)} \left(\frac{(1-2\nu)(\delta_{ik} \delta_{jn} + \delta_{jk} \delta_{in}) - (1-4\nu) \delta_{ij} \delta_{kn}}{r^3} \right. \\ & + 3 \frac{\nu(\delta_{ik} r_j r_n + \delta_{jk} r_i r_n + \delta_{in} r_j r_k + \delta_{jn} r_i r_k) + (1-2\nu)(\delta_{kn} r_i r_j + \delta_{ij} r_k r_n)}{r^5} \\ & \left. - 15 \frac{r_i r_j r_k r_n}{r^7} \right) \quad (3-37) \end{aligned}$$

The notation in Equations 3-34 to 3-37 is confusing but allows the kernels to be written very concisely. They are written in terms of a coordinate system aligned with the fracture plane of the displacement discontinuity. The variable D_{kn} represents the displacement in the k direction relative to a plane with normal n . The coefficient G_{ijkn} represents the displacement in the i direction caused by a displacement discontinuity in the k direction where the discontinuity occurs on a plane with a normal vector n . The indices i, j , and k each cycle through three directions: one corresponds to a direction normal to the fracture plane and two correspond to orthogonal directions that are aligned with the fracture plane. The index n does not cycle and always represents the direction that is the normal to the fracture plane. δ_{ij} is the Kronecker delta as described in Appendix A, where it equals zero if $i \neq j$ and equals one if $i = j$.

Note that Equations 3-34 to 3-37 are calculated in terms of the local fracture coordinate system. When calculating the effect of one fracture's displacement discontinuity on another fracture (whose displacement discontinuities are given in a different coordinate system), the interaction coefficients must be rotated accordingly.

Calculation of interaction coefficients for an element with itself is a special challenge because the kernels have a singularity for $r=0$, that is, if the distance between the element being affected and the displacement is zero. In this case, special care must be taken to evaluate the integral numerically to remove the singularity. These techniques are discussed in Aliabadi (2002).

A good explanation of the three-dimensional displacement discontinuity method is also found in Wiles and Curran (1982). For the two-dimensional displacement discontinuity kernels, see Crouch and Starfield (1983).

3.4.6. Coulomb Failure and the Displacement Discontinuity Method

Applying the Displacement Discontinuity (DD) method to Coulomb failure is not straightforward. The DD method was designed to model open fractures, fractures whose walls are not touching. If the normal stress is compressive rather than tensile, the DD method predicts that the walls interpenetrate. What would happen in reality is that the walls would come in contact and resist further displacement. The normal stress on either side of the fracture would balance, preventing interpenetration, and friction would prevent shear displacement. Since there is no displacement in the case of frictional sticking, nothing is happening and the DD method does not need to be applied.

There are two possible situations when the DD would be applied: fracture opening and fracture sliding.

A fracture will open if the effective normal stress is tensile. That would take place if the pore pressure exceeded the normal stress imposed by the remote loading. The displacement of each fracture affects the others, so all the opening elements must be included in a system of equations and solved simultaneously. Opening of fractures is sometimes referred to as “jacking.”

The difficulty is that it is not known ahead of time which fractures are open. The opening fractures perturb the stress around them, which might cause other closed fracture to open or open fractures to close. In the second case, the system of equations can be solved, yet the solution to the system would predict some of the walls interpenetrating. Ghassemi (2007) included all elements in the system, but applied “penalty stresses” on the fractures which interpenetrated. He solved the system, applied penalty stresses, and iterated until convergence. This approach increased the computational cost of solving the problem. Another approach, never applied in an EGS application, is to transform the DD problem to be a “complementarity” problem. This is a class of problem found in a variety of applications in economics, robotics, and other fields. These problems can be solved using specialized algorithms. Examples of this approach are Mutlu and Pollard (2008) and De Bremaecker et al. (2000). This approach appears to be the most efficient and stable way of solving these problems.

It is unclear that jacking occurs in EGS stimulation, at least at Soultz. This issue is addressed at length in Section 3.5. To summarize, it is generally believed that during some stimulations, jacking occurs at the top of the open hole sections (Cornet, 2007). This study argues that the evidence for jacking is inconclusive. Even if it did occur during some of the stimulations, it occurred only in a section of the reservoir and not during all the stimulations. The original version of the simulator probably will not include jacking, but it may be included at a later time.

A similar difficulty is faced with fracture shear. It is not known *a priori* which fractures are going to shear. Based on pore pressures from the fluid flow solution, a certain number of elements might be identified as exceeding the failure criterion. But when those elements displace, the affect of their slip might cause other fractures to exceed the

failure criterion. The slip of those new fractures would affect the stress on the original fractures, and so on.

Fractures fail in shear when their shear traction exceeds the frictional force resisting shear. To determine the displacement of the fractures that fail in shear, displacements must be found such that the shear forces again equal the friction resistance. It may be that when the fracture is failing the frictional resistance temporarily is lowered because dynamic friction is lower than static friction. Or after the first failure, friction may be permanently reduced. Either effect could be included.

This study would propose the following scheme to handle fracture shear. Given a set of fractures known to exceed the failure criterion, a system of equations can be set up such to solve for displacements that bring the elements back into frictional equilibrium. Once the displacements are found, the stress perturbations on nearby fractures are calculated, and if any of the fractures exceed the failure criterion, they are included in the system of equations. The process is repeated until all the failing fractures are included.

Any time that iteration is used, computational difficulty increases. However fracture slip is not likely to require a huge amount of computational effort. On any given time step, only a small number of fractures should be shearing. Once a fracture shears, it may not shear again for a long time. This is in contrast to opening fractures, which, once opened, would be unlikely to close and thus would be included in all future opening calculations. Iteration on a relatively small number of fracture elements each time step should not be prohibitive as long as there are not convergence difficulties.

To update the fracture transmissibility, some correlation will be used to relate magnitude of slip to transmissibility or permeability. Examples of such correlations are in Kohl and Mège (2007), Bruel (2007) and others. Fracture transmissibility and pore volume can also be correlated to normal stress (which in turn depends on both temperature and pressure) to account for fracture compliance. This effect could be incorporated implicitly in the mass and energy flow equations or be updated explicitly during the shear failure calculation step.

3.4.7. Heat Conduction in the Volume

In some cases, BEM can be applied successfully to handle unsteady heat conduction without needing to discretize the volume. Unfortunately, for use in the problem considered in this paper, this is not possible. This section will explain why and propose that at short time scales, a one-dimensional approximation is adequate.

Heat transport through the granite occurs by conduction, which is governed by Fourier's law of heat conduction (Wrobel 2002):

$$\nabla^2 T = \frac{1}{k_t} \frac{\partial T}{\partial t} \quad (3-38)$$

where k_t is the thermal diffusivity, $k_t = \frac{K}{\rho c}$, where K is the thermal conductivity, c is the heat capacity, and ρ is the density. It is assumed that there is negligible fluid flow in the volume, so convection can be ignored.

Unsteady-state heat flow is related to Poisson's Equation, which is (Brebbia and Dominguez, 1992):

$$\nabla^2 v = a \quad (3-39)$$

where a is a source term. The BEM formulation of Poisson's equation is:

$$v(\mathbf{x}') + \int_S w^*(\mathbf{x}', \mathbf{x}) v(\mathbf{x}) dS = \int_S v^*(\mathbf{x}', \mathbf{x}) w(\mathbf{x}) dS + \int_V v^*(\mathbf{x}', \mathbf{X}) a(\mathbf{X}) dV \quad (3-40)$$

where:

$$w(\mathbf{x}) = \frac{\partial v}{\partial n} = \frac{\partial v}{\partial n_1} n_1 + \frac{\partial v}{\partial n_2} n_2 + \frac{\partial v}{\partial n_3} n_3 \quad (3-41)$$

This is the equivalent of Somigliana's equation for a potential problem. v is the fundamental solutions to the potential problem, and w is the derivative of v with respect to the normal. The kernels can be found in Wrobel (2002).

If there are no heat sources in the body, the volume integral term disappears and the problem simplifies to the Laplace equation, which also describes steady state heat flow:

$$\nabla^2 v = 0 \quad (3-42)$$

In the case of unsteady state flow, a Laplace transform can be applied to put the problem into the same form as the BEM formulation of Poisson's equation. The transformation is:

$$L[T(\mathbf{x}, t)] = Y(\mathbf{x}, s) = \int_0^{\infty} T(\mathbf{x}, t) e^{-st} dt \quad (3-43)$$

The problem is transformed to (Wrobel 2002):

$$\nabla^2 Y(\mathbf{x}, s) - \frac{s}{k_t} Y(\mathbf{x}, s) - \frac{1}{k_t} T_{init}(\mathbf{x}) = 0 \quad (3-44)$$

Where T_{init} is the initial temperature distribution. A fundamental solution exists for this equation:

$$Y^*(\mathbf{x}', \mathbf{x}, s) = \frac{(k_t s)^{1/4}}{r^{1/2} (2\pi k_t)^{3/2}} K_{1/2} \left[\frac{s^{1/2} r}{k_t^{1/2}} \right] \quad (3-45)$$

Where $K_{1/2}$ is the modified Bessel function of the second kind of order $1/2$. The boundary integral formation is:

$$Y(x', s) + \int_S Z^*(\mathbf{x}', \mathbf{x}, s) Y(\mathbf{x}, s) dS = \int_S Y^*(\mathbf{x}', \mathbf{x}, s) Z(\mathbf{x}, s) dS + \frac{1}{k_t} \int_V Y^*(\mathbf{x}', \mathbf{x}, s) T_{init}(\mathbf{x}) dV \quad (3-46)$$

Where Z^* is the derivative of Y^* , and Z is the derivative of Y . Note the similarity to the Poisson boundary integral formulation. The initial temperature distribution acts like a body force when the unsteady state heat conduction problem is transformed to Laplace space. If the initial temperature is constant, the volume integral can be eliminated through a simple variable transformation. Define a variable η , which is the difference between the current temperature and the initial temperature:

$$\eta(\mathbf{x}, t) = T(\mathbf{x}, t) - T_{init} \quad (3-47)$$

$\eta(\mathbf{x}, 0) = 0$ everywhere. Therefore, the volume integral goes to zero for the Laplace space boundary integral formulation. The problem can be solved like any other boundary element problem. The transformation back to the time variable can be done by an inverse Laplace transform algorithm. This technique is used by Ghassemi (2007) to solve a coupled fluid-heat-elasticity problem for a single fracture using BEM. However, it required him to make the assumption that the flow distribution in the fracture does not change with time.

This is a simplification that cannot be made in the stimulation model envisaged in this study because the flow field will change dramatically over the course of the simulation because of permeability enhancement with shear failure. There is no way to integrate the fluid flow into the boundary element in this case. Instead, the solution would have to use time steps and alternate between solving the flow and heat problems. At each step, the solver would solve for the flow distribution in the fractures, then solve for the heat flow out of those fractures based on that solution. The stability of such an explicit scheme would be questionable. Worse, this scheme would require that the unsteady state BEM problem be solved over and over with changing initial conditions at each time step. The

volume integral cannot be avoided using a variable transformation because the initial condition is not constant.

An alternate solution to the unsteady state heat conduction problem avoids the Laplace transform by using a time-dependent fundamental solution. Unfortunately this problem also requires a volume integral that cannot be eliminated unless there is a constant temperature initial condition (Wrobel, 2002).

Solving a volume integral requires discretizing the volume, which is undesirable. The advantage of BEM is lost, and it is not clear whether BEM would be any better than other methods such as finite difference. Finite difference could solve the problem implicitly, but would also require discretizing the volume and might suffer from numerical difficulties associated with large contrasts in transmissibility.

Instead it is proposed to use a simple one-dimensional approximation. At short times scales, this is an accurate approximation. Formulations exist that allow one-dimensional heat conduction to be included implicitly.

The one-dimensional solution to unsteady-state heat conduction equation (which is the same as the diffusivity equation, just with different variables) is given by Equation 2-21:

$$\frac{T - T_{init}}{T_b} = 1 - \operatorname{erf} \left(\frac{x}{\sqrt{4k_t t}} \right) \quad (3-48)$$

where k_t is the thermal diffusivity, T_{init} is the initial temperature and T_b is the temperature at the boundary. A typical value of thermal diffusivity for granite is $10^{-6} \text{ m}^2/\text{sec}$. After three days, the distance from a fracture where the temperature has increased by just 10% of the difference between the applied temperature and the fracture temperature is only 1.2m. After 30 years the distance is 71m. On a time scale of 30 years, fracture thermal interaction might matter. On a time scale of a few days for stimulation, it would not.

The solution to Equation 3-48 assumes a constant initial temperature. In the simulator envisioned here, the fracture temperature will change with time. The same problem exists here as existed in the BEM formulation: the initial condition changes at each time step. The popular non-isothermal reservoir simulator TOUGH2 (Pruess et al. 1999) uses a solution proposed by Vinsome and Westerveld (1980).

Vinsome and Westerveld proposed a simple trial function for the temperature distribution in the rock:

$$T(t, x) = (\theta + p_c x + q_c x^2) e^{-x/d} \quad (3-49)$$

where p_c and q_c are parameters to be determined, d is a diffusion length, which equals $\sqrt{k_t t} / 2$, x is the distance from the fracture, and θ is the temperature at the interface.

Vinsome and Westerveld enforce conservation of energy and satisfaction of the diffusivity equation at the interface. They also use an implicit finite difference discretization of time to derive the heat loss rate:

$$Q^{n+1} = -K \frac{\partial T}{\partial x}(x=0) = K \left(\frac{\theta^{n+1}}{d^{n+1}} - p_c^{n+1} \right) \quad (3-50)$$

Where K is the thermal conductivity. The additional parameters needed in the calculation are defined as:

$$p_c = \frac{\frac{k_i \Delta t \theta^{n+1}}{d^{n+1}} + I^n - \frac{(d^{n+1})^3 (\theta^{n+1} - \theta^n)}{k_i \Delta t}}{3(d^{n+1})^2 + k_i \Delta t} \quad (3-51)$$

$$q_c = \frac{2p_c^{n+1} d^{n+1} - \theta^{n+1} + (d^{n+1})^2 \frac{\theta^{n+1} - \theta^n}{k_i \Delta t}}{2d^2} \quad (3-52)$$

$$I^n = \theta^n d^n + p_c^n (d^n)^2 + 2q_c^n (d^n)^3 \quad (3-53)$$

The superscript n indicates a value from the previous time step. Superscript $n+1$ indicates the time step being calculated. Δt is the length of the time step. Note that in the calculation of d at each time step, the time variable t is not reset. The time is calculated as the time from the beginning of simulation. These equations allow for one-dimensional heat flow with varying boundary condition to be calculated implicitly in a reservoir simulator and need only the calculation of a few parameters. Testing in Vinsome and Westerveld (1980) indicated good accuracy even during cyclic injection of hot and cold water.

3.4.8. Thermoelasticity

Cooling in the rock volume causes the rock to contract. The effect on stress in a solid due to thermal effects is described by the theory of thermoelasticity. Only a brief overview of thermoelasticity is given here. In the conduction equation, stresses introduce an extra term to take into account the changes in strain energy (the conduction equation is really an energy balance) (Jaeger, 2007):

$$\nabla^2 T = \frac{1}{k_i} \frac{\partial T}{\partial t} + \frac{3K_r \beta T_{init}}{\rho c} \frac{\partial \varepsilon_b}{\partial t} \quad (3-54)$$

Where ε_b is the bulk strain, β is the coefficient of linear thermal expansion (units $1/^\circ\text{K}$), ρ is the density of the rock, c is the specific heat, T_{init} is the initial temperature (in absolute temperature), and K_r is the macroscopic bulk modulus (units $1/\text{pressure}$). In most cases,

the magnitude of the far right term is very small compared to the other terms. This is the case if:

$$\frac{9K_r \beta^2 T_{init}}{\rho c} \ll 1 \quad (3-55)$$

Typical values for granite are $\beta = 4.7 \times 10^{-5}$ (1/°K), $\rho c = 1.9 \times 10^6$ (J/(°K-m³)), and $K_r = 25$ GPa. T_{init} is the reference temperature. Taking $T_{init} = 473^\circ\text{K}$, gives the value on the left side of Equation 3-55 equals 0.001. Omitting the strain energy from the temperature equation is a very reasonable approximation and makes the problem much simpler.

If strain is omitted from the energy equation, the temperature field can be solved and then substituted into the strain-stress equation. The compressive stresses are affected by a bulk strain, which is proportional to the temperature gradient. Temperature does not affect the shear stress. The modified Hooke's law is:

$$\sigma_{ij} = \lambda \delta_{ij} \epsilon_{kk} + 2\mu_s \epsilon_{ij} + 3\delta_{ij} \beta K_r (T - T_{init}) \quad (3-56)$$

In order to calculate thermoelastic stress, the equation for thermoelastic potential, Φ , can be solved (Nowacki, 1986).

$$\nabla^2 \Phi = \frac{1+\nu}{1-\nu} \beta \times \Delta T \quad (3-57)$$

Once Φ is known, stresses can be calculated according to the equation:

$$\sigma_{ij} = 2\mu \left(\frac{\partial^2 \Phi}{\partial x_i \partial x_j} - \frac{1+\nu}{1-\nu} \beta \times \Delta T \right) \quad (3-58)$$

These equations can be solved using numerical methods.

Chapter 4

4. Future Work

This report lays the foundation for future work. The first step is to write the simulator described in Chapter 3. The simulator will facilitate study of many topics. These include (1) novel strategies for stimulation design, (2) wellbore orientation and spacing, (3) prediction of life of a reservoir, (4) sensitivity study on the effect of various parameters, (5) prediction of intensity and location of microseismic events, (6) identification of geological settings that are advantageous for EGS.

Another topic of further work is the generation of discrete fracture models that are geologically realistic for EGS. It is obvious that the geometry of the preexisting fracture network has a profound impact on EGS reservoirs, and there is much work left to do to characterize their properties and generate realistic three-dimensional realizations. Details such as the nature of fracture intersections need to be better addressed.

Describing coupled thermal and mechanical effects in conjunction with realistic geology will lead to much more powerful predictive models of EGS systems.

Nomenclature

| | | |
|------------|---|---|
| a | = | Source term in Poisson's equation |
| A_{pm} | = | Area of the interface between elements p and m |
| b_i | = | Body force |
| c_t | = | Total compressibility |
| c | = | Heat capacity |
| C_{ij} | = | Term in BEM formation to account for points on the boundary |
| Cd_{pm} | = | Conduction between elements p and m |
| Cv_{pm} | = | Convection between elements p and m |
| D_{pm} | = | Sum of the distances between the center of element p and m and the interface between the two elements |
| D_{in} | = | Displacement discontinuity on a plane with normal n |
| d | = | Heat diffusive length used in one-dimensional conduction approximation |
| e_m | = | Energy source term in element m |
| E_m | = | Bulk enthalpy density of element m |
| F_{pm} | = | Mass flow rate between elements p and m |
| g_i | = | Weighting factor in Gaussian quadrature numerical integration |
| g_{pm} | = | Component of gravitational acceleration between element p and m |
| G_{ikn} | = | Interaction coefficient for displacement in displacement discontinuity problem |
| H_{ijkn} | = | Interaction coefficient for stress in displacement discontinuity problem |
| I | = | Coefficient used in one-dimensional conduction approximation |
| k | = | Permeability |
| k_t | = | Thermal diffusivity |
| K | = | Thermal conductivity |
| K_r | = | Bulk modulus |
| M_m | = | Mass per bulk volume in element m |
| M_{kij} | = | Stress equation interaction coefficient |
| P | = | Pressure |
| P_{init} | = | Initial pressure |
| P_{inj} | = | Injection pressure |

| | | |
|-------------|---|--|
| P_D | = | Dimensionless pressure |
| \bar{P}_D | = | Laplace space dimensionless pressure |
| P_b | = | Boundary pressure |
| p_c | = | Coefficient used in one-dimensional conduction approximation |
| q_c | = | Coefficient used in one-dimensional conduction approximation |
| q_m | = | Mass source term in element m |
| Q | = | Heat flux |
| r | = | Radius |
| r_D | = | Dimensionless radius |
| r_w | = | Wellbore radius |
| s | = | Laplace variable |
| S | = | Arbitrary Surface |
| S_{hmin} | = | Least horizontal stress |
| S_{Hmax} | = | Greatest horizontal stress |
| S_o | = | Cohesion |
| S_v | = | Vertical stress |
| S_{kij} | = | Stress equation interaction coefficient |
| T | = | Temperature |
| T_{init} | = | Initial temperature |
| T_b | = | Temperature at the boundary |
| t | = | Time |
| t_D | = | Dimensionless time |
| t_i | = | Traction |
| t^* | = | Traction fundamental solution |
| T_{ij} | = | Traction interaction coefficient |
| u_i | = | Displacement |
| u^* | = | Displacement fundamental solution |
| U_{ij} | = | Displacement interaction coefficient |
| V_m | = | Volume of element m |
| v | = | Variable used in Poisson's equation |
| v^* | = | Fundamental solution to Poisson's problem |
| w | = | Derivative of v, the variable used in Poisson's equation |
| w^* | = | Derivative of the fundamental solution to Poisson's equation |
| x | = | Distance |
| x_i | = | Coordinate direction |

| | | |
|--------------------|---|---|
| Y | = | Laplace transform of temperature |
| Y^* | = | Fundamental solution of Laplace transform of the heat conduction equation |
| Z | = | Derivative of the Laplace transform of temperature |
| Z^* | = | Derivative of the fundamental solution of the Laplace transform of the heat conduction equation |
| z | = | Vertical distance |
| α | = | Hydraulic diffusivity |
| β | = | Linear coefficient of thermal expansion |
| β_f | = | Orientation of failure plane |
| γ | = | Gravitational constant |
| δ_{ij} | = | Kronecker delta |
| ε_{ij} | = | Strain |
| ε_b | = | Strain |
| η | = | Change in temperature from initial temperature |
| θ | = | Temperature at the boundary in one-dimensional heat conduction |
| θ_m | = | Temperature of element m |
| λ | = | Lamé Constant |
| μ | = | Coefficient of friction |
| μ_l | = | Viscosity |
| μ_m | = | Shear modulus |
| ρ_m | = | Density of fluid in element m |
| σ_n | = | Effective Normal stress |
| σ_n | = | Normal stress |
| σ_{ij} | = | Stress |
| σ_1 | = | Greatest principal stress |
| σ_2 | = | Intermediate principal stress |
| σ_3 | = | Least principal stress |
| τ | = | Shear stress |
| ν | = | Poisson's ratio |
| ξ_i | = | Directional coordinate in a triangular coordinate system |
| φ | = | Porosity |
| Φ | = | <i>Thermoelastic potential</i> |
| \mathbf{A} | = | Vector of unknowns in mixed boundary condition displacement problem |
| \mathbf{n} | = | Normal vector |

| | | |
|----------------------|---|--|
| p | = | Traction vector |
| t_b | = | Vector of tractions |
| T | = | Stress tensor |
| T_b | = | Matrix of traction interaction coefficients |
| u | = | Darcy velocity vector (distance per second) |
| u_b | = | Vector of displacements |
| U_b | = | Matrix of displacement interaction coefficients |
| x | = | Vector of unknowns in mixed boundary condition displacement problem |
| y | = | Vector of boundary conditions in mixed boundary condition displacement problem |

References

- Acuna, J. and Y. Yortsos. "Application of fractal geometry to the study of networks of fractures and their pressure transient." *Water Resources Research*. 31(3):527-540, 1995.
- Aliabadi, M.H. The Boundary Element Method. Vol. 2. West Sussex, England: John Wiley & Sons, Ltd., 2002.
- Armand, G., M. Boulon, N. Hoteit, and S. Cannic. "Mechanical behavior of natural joints of granodiorite under high normal stress." Hans-Peter Rossmann, ed. Mechanics of Jointed and Faulted Rock 3. Rotterdam: Balkema, 1998, 217-222.
- Auradou, Harold, German Drazer, Alejandro Boschan, Jean-Pierre Hulin, and Joel Koplik. "Flow channeling in a single fracture induced by shear displacement." *Geothermics*. 35:576-588, 2006.
- Bachler, D., K. Evans, R. Hopkirk, T. Kohl, T. Mégel, and L. Rybach. "Data analysis and controls toward understanding reservoir behavior and the creation of a conceptual reservoir model." EU Project No. JOR3-CT 98-0313 (DG12-WSM), 2000.
- Bankwitz, P. and E. Bankwitz. "Event related jointing in rocks on Bornholm island (Denmark)." *Zeitschrift für Geologische Wissenschaften*. 22(1/2): 97-114, 1994.
- Bankwitz, P., E. Bankwitz, R. Thomas, K. Wemmer, and H. Kämpf. "Age and depth evidence for pre-exhumation joints in granite plutons: fracturing during the early cooling stage of felsic rock." Cosgrove, J.W. and T. Engelder (eds). The Initiation, Propagation, and Arrest of Joints and Other Fractures. Geological Society of London, Special Publications, 231: 25-47, 2004a.
- Bankwitz, P. and E. Bankwitz. "The relationship of tilt and twist of fringe cracks in granite plutons." Cosgrove, J.W. and T. Engelder (eds). The Initiation, Propagation, and Arrest of Joints and Other Fractures. Geological Society of London, Special Publications, 231: 183-208, 2004b.
- Baria, R., S. Michelet, J. Baumgaertner, B. Dyer, A. Gerard, J. Nicholls, T. Hettkamp, D. Teza, N. Soma, H. Asanuma, J. Garnish, and T. Megel. "Microseismic monitoring of the world's largest potential HDR reservoir." *Proceedings, Twenty-Ninth Workshop on Geothermal Reservoir Engineering*, Stanford University, 2004.
- Baria, R., Sophie Michelet, Joerg Baumgärtner, Ben Dyer, Jonathan Nicholls, Thomas Hettkamp, Dimitra Teza, Nobukaza Soma, Hiro Asanuma, John Garnish, and Thomas Megel. "Creation and mapping of 5000m deep HDR/HFR reservoir to produce electricity." *Proceedings World Geothermal Congress*, 2005.
- Baria, R., R. Jung, T. Tischner, J. Nicholls, S. Michelet, B. Sanjuan, N. Soma, H. Asanuma, B. Dyer, and J. Garnish. "Creation of an HDR Reservoir at 5000m

- depth at the European HDR project.” *Proceedings, Thirty-First Workshop on Geothermal Reservoir Engineering*, Stanford University, 2006.
- Barton, N. “The shear strength of rock and rock joints.” *International Journal of Rock Mechanics and Mining Sciences*. 13: 255-279, 1976.
- Baumgartner, J., A. Gérard, R. Baria, R. Jung, T. Tran-Viet, T. Gandy, L. Aquilina, and J. Garnish. “Circulating the HDR reservoir at Soultz: maintaining production and injection flow in complete balance.” *Proceedings, Twenty-Third Workshop on Geothermal Reservoir Engineering*, Stanford University, 1998.
- Bergbauer, Stephan and Stephan Martel. “Formation of joints in cooling plutons.” *Journal of Structural Geology*. 21:821-835, 1999.
- Bird, B. W. Stewart, and E. Lightfoot. Transport Phenomena. New York: John Wiley & Sons, Inc., 2007.
- Brebbia, C. and J. Dominguez. Boundary Elements: An Introductory Course. Southampton, U.K.: Computational Mechanics Publications, 1992.
- Bruel, Dominique. “Using the migration of the induced seismicity as a constraint for fractured hot dry rock reservoir modeling.” *International Journal of Rock Mechanics & Mining Sciences*. 44:1106-1117, 2007.
- Bürgmann, R., D. Pollard, and S. Martel. “Slip distributions on faults: effects of stress gradients, inelastic deformation, heterogeneous host-rock stiffness, and fault interaction.” *Journal of Structural Geology*. 16(12):1675-1690, 1994.
- Byerlee, James. “Friction of rocks.” *Pure and Applied Geophysics*. 116:615-626, 1978
- Byerlee, James. “Frictional Characteristics of Granite under High Confining Pressure.” *Journal of Geophysical Research*. 72(14):3639-3648, 1967.
- Chen, A., S.P. Narayan, Z. Yang, and S.S. Rahman. “An experimental investigation of hydraulic behavior of fractures and joints in granitic rock.” *International Journal of Rock Mechanics*. 37:1061-1070, 2000.
- Childs, C., A. Nicol, J. Walsh, and J. Watterson. “Growth of vertically segmented normal faults.” *Journal of Structural Geology*. 18(12): 1389-1397, 1996.
- Commons.wikimedia.org. “File: Fracture modes v2.svg.” <http://commons.wikimedia.org/wiki/File:Fracture_modes_v2.svg>. Accessed 22 Aug. 2009.
- Cornet, F.H., T. Bérard, and S. Bourouis. “How close to failure is a granite rock mass at a 5km depth?” *International Journal of Rock Mechanics & Mining Sciences*. 44:47-66, 2007.
- Crouch, S.L. and A.M. Starfield. Boundary Element Methods in Solid Mechanics. London, U.K.: George Allen & Unwin (Publishers), Ltd., 1983.
- Cuenot, N., J. Charléty, L. Dorbath, H. Haessler. “Faulting mechanisms and stress regime at the European HDR site of Soultz-sous-Forêts, France.” *Geothermics*. 35: 561-575, 2006.

- De Bremaecker, J.-Cl., M.C. Ferris, and D. Ralph. "Compressional fractures considered as contact problems and mixed compementarity problems." *Engineering Fracture Mechanics*. 66: 287-303, 2000.
- dell'Erba, D. Thermoelastic Fracture Mechanics using Boundary Element. Southampton, U.K.: WIT Press, 2002.
- Dezayes, C., A. Genter, and G. Hooijkaas. "Deep-seated geology and fracture system of the EGS Soultz reservoir (France) based on recent 5km depth boreholes." *Proceedings World Geothermal Congress*, 2005.
- Economides, M., and T. Martin, eds. Modern Fracturing: Enhancing Natural Gas Production. Houston, TX: Energy Tribute Publishing, Inc., 2007.
- Ehlig-Economides, C. "Well test analysis for wells produced at a constant pressure." PhD Thesis, Stanford University, 1979.
- El Ouahed, A.K., D. Tiab, A. Mazouzi, S. Jokhio. "Application of artificial intelligence to characterize naturally fractured reservoirs." SPE 84870, 2003.
- Energy Information Administration. "International Energy Statistics: Official Energy Statistics from the U.S. Government." <<http://www.eia.doe.gov/emeu/international/contents.html>>. Accessed 23 Aug 2009.
- Esaki, T., S. Du, Y. Mitani, K. Ikusada, L. Jing. "Development of a shear-flow test apparatus and determination of coupled properties for a single rock joint." *International Journal of Rock Mechanics*, 36:641-650, 1999).
- Evans, K., A. Genter, and J. Sausse. "Permeability creation and damage due to massive fluid injections into granite at 3.5km at Soultz: 1. Borehole observations." *Journal of Geophysical Research*. 110:B04203, 2005.
- Evans, K. "Pemeability creation and damage due to massive fluid injections into granite at 3.5km at Soultz: 2. Critical stress and fracture strength." *Journal of Geophysical Research*. 110: B04204, 2005.
- Evans, K., H. Moriya, H. Niitsuma, R. Jones, W. Phillips, A. Genter, J. Sausse, R. Jung, and R. Baria. "Microseismicity and permeability enhancement of hydrogeologic structures during massive fluid injections into granite at 3 km depth at the Soultz HDR site." *Geophysical Journal International*. 160: 388-412, 2005.
- "FracMan7: User Documentation." Golder Associates, Inc., 2009.
- Genter, A., D. Fritsch, N. Cuenot, J. Baumgartner, and J. Graff. "Overview of the current activities of the European EGS Soultz Project: From exploration to electricity production." *Proceedings, Thirty-Fourth Workshop on Geothermal Reservoir Engineering*, Stanford University, 2009.
- Genter, Albert and Herve Traineau. "Analysis of macroscopic fractures in granite in the HDR geothermal well ESP-1, Soultz-sous-Forêts, France." *Journal of Volcanology and Geothermal Research*. 72: 121-141, 1996.
- Ghassemi, A., S. Tarasovs, and A.H.-D. Cheng. "A 3-D study of the effects of thermomechanical loads on fracture slip in enhanced geothermal reservoirs."

- International Journal of Rock Mechanics and Mining Sciences*. 44: 1132-1148, 2007.
- Glanz, James. "Deep in bedrock, clean energy and quake fears." *The New York Times*. 23 June 2009.
- Glanz, James. "Quake fears stall energy extraction project." *The New York Times*. 13 July 2009.
- Goovaerts, P. Geostatistics for Natural Resource Evaluation. New York: Oxford University Press, 1997.
- Granier, Therese. "Origin, damping, and pattern of development of faults in granite." *Tectonics*. 4(7): 721-737, 1985.
- Haimson, B.C. and I.S. Song. "A new borehole failure criterion for estimating *in situ* stress from breakout span." *Proceedings 8th International Congress Rock Mechanics*, Vol. 1. T. Fujii, ed. Balkema Rotterdam, (1995), 341-346.
- Henriksen, A. "Fracture interpretation based on electrical and acoustic borehole image logs." BRGM/RP-50835-FR, 2001.
- Hoffman, W., W. Dunne and M. Mauldon. "Probabilistic-mechanistic simulation of bed-normal joint patterns." Cosgrove, J.W. and T. Engelder (eds). The Initiation, Propagation, and Arrest of Joints and Other Fractures. Geological Society of London, Special Publications. 231: 269-283, 2004.
- Horne, Roland. Modern Well Test Analysis. 2nd Ed. Palo Alto, CA: Petroway, 1995.
- Hossain, M., M. Rahman, S. Rahman. "A shear dilation stimulation model for production enhancement from naturally fractured reservoirs." SPE 78355, 2002.
- Intergovernmental Panel on Climate Change. "Climate change 2007: synthesis report contribution of working groups I, II, and III to the Fourth Assessment Report of the Intergovernmental Panel on Climate Change." R. Pachauri and A. Reisinger, eds. Geneva, Switzerland: IPCC, 2007.
- Ito, T., and M. D. Zoback. "Fracture permeability and in-situ stress to 7 km depth in the KTB Scientific Drillhole." *Geophysics Research Letters*, 27:1045-1048 2000.
- Jaeger, J.C., N.G.W. Cook and R.W. Zimmerman. Fundamentals of Rock Mechanics. Malden, MA: Blackwell Publishing, 2007.
- Karimi-Fard, M., L.Durlowsky, and K. Aziz. "An efficient discrete fracture model applicable for general purpose reservoir simulators." SPE 88812, 2004.
- Kohl, T., and R.J. Hopkirk. "'FRACTure' – a simulation code for forced flow and transport in fractured, porous rock." *Geothermics*, 19(1)1: 3-15, 1995.
- Kohl, T. and T. Mégel. "Coupled hydro-mechanical modelling of the GPK3 reservoir Stimulation at the European EGS Site Soultz-Sous-Forêts." *Proceedings: Thirtieth Workshop on Geothermal Reservoir Engineering*, Stanford University, 2005.
- Kohl, T. and T. Mégel. "Predictive modeling of reservoir response to hydraulic stimulations at the European EGS site Soultz-sous-Forêts." *International Journal of Rock Mechanics and Mining Sciences*. 44: 1118-1131, 2007.

- Kovac, K.M., Susan J. Lutz, Peter Drakos, Joel Byersdorfer, and Ann Robertson-Tait. "Borehole image analysis and geological interpretation of selected features in Well DP 27-15 at Desert Peak, Nevada: pre-stimulation evaluation of an Enhanced Geothermal System." *Proceedings, Thirty Fourth Workshop on Geothermal Engineering*, Stanford University, 2009.
- Lund, J. "100 Years of Geothermal Power Production." *GHC Bulletin*, September 2004, 11-19.
- Maerten, L., E. Willemse, D. Pollard, and K. Rawnsley. "Slip distributions on intersecting normal faults." *Journal of Structural Geology*. 21: 259-271, 1999.
- Martel, S.J. "Formation of compound strike-slip fault zones, Mount Abbot quadrangle, California." *Journal of Structural Geology*. 12(7): 869-882, 1990.
- Martel, S. and W. Boger. "Geometry and mechanics of secondary fracturing around small three-dimensional faults in granitic rock." *Journal of Geophysical Research*. 103(B9): 21,299-21,314, 1998.
- MathWorks, Inc. Matlab and Simulink: Getting Started with Matlab. Natick, MA: MathWorks, Inc., 2007.
- McTigue, D.F. "Thermoelastic response of fluid-saturated porous rock." *Journal of Geophysical Research*. 91(B9): 9533-9542, 1986.
- Mutlu, O. and D.D. Pollard. "On the patterns of wing cracks along an outcrop scale flaw: A numerical modeling approach using complementarity." *Journal of Geophysical Research*. 113: B06403, 2008.
- Norton, D., H.P. Taylor, Jr., and Dennis Bird. "Geometry and high-temperature brittle deformation of the Skaergaard Intrusion." *Journal of Geophysical Research*. 89(B12): 10,178-10,192, 1984.
- Okabe, T., and K. Hayashi. "Estimation of stress field by using drilling-induced tensile fractures observed at well TG-2 and a study of critically-stressed shear fractures based on stress field." *World Geothermal Congress*, ed. E. Iglesias, Morioka, Japan, May 28th-June 10th, 1533-1538, International Geothermal Association, 2000.
- Olson, J. and D. Pollard. "The initiation and growth of en échelon veins." *Journal of Structural Geology*. 13(5): 595-608, 1991.
- Olsson, W.A. and S.R. Brown. "Hydromechanical response of a fracture undergoing compression and shear." *International Journal of Rock Mechanics*, 30: 845-851, 1993.
- Papaliangas, T., S. Hencher, A. Lumsden, and S. Manolopoulou. "The effect of frictional fill thickness on the shear strength of rock discontinuities." *International Journal of Rock Mechanics and Mining Sciences and Geomechanical Abstracts*. 3(2): 81-91, 1993.
- Pollard, D. and Raymond Fletcher. Fundamentals of Structural Geology. Cambridge, UK: Cambridge University Press, 2008.

- Pruess, Karsten, Curt Oldenburg, and George Moridis. "TOUGH2 User's Guide, Version 2.0." Earth Sciences Division, Lawrence Berkeley National Laboratory, 1999.
- Rahman, M.K., M.M. Hossain, and S.S. Rahman. "A shear-dilation-based model for evaluation of hydraulically stimulated naturally fractured reservoirs." *International Journal for Numerical and Analytical Methods in Geomechanics*. 26: 469-497, 2002.
- Railroad Commission of Texas. "Barnett Shale Information." <<http://www.rrc.state.tx.us/barnettshale/>>. Accessed 23 Aug 2009.
- Renshaw, C. and D. Pollard. "Numerical simulation of fracture set formation: A fracture mechanics model consistent with experimental observations." *Journal of Geophysical Research*. 99(B5): 9359-9372, 1994.
- Sanjuan, B., J. Pinault, P. Rose, A. Gérard, M. Brach, G. Braibant, C. Crouzet, J. Foucher, A. Gautier, and S. Touzelet. "Tracer testing of the geothermal heat exchanger at Soultz-sous-Forêts (France) between 2000 and 2005." *Geothermics*. 35: 622-653, 2006.
- Sanyal, S. "Cost of Geothermal Power and Factors that Affect It." *Proceedings World Geothermal Congress*, 2005.
- Sausse, J., C. Dezayes, A. Genter, and A. Bisset. "Characterization of fracture connectivity and fluid flow pathways derived from geological interpretation and 3D modelling of the deep seated EGS reservoir of Soultz (France)." *Proceedings, Thirty-Third Workshop on Geothermal Reservoir Engineering*, Stanford University, 2008.
- Segall, P. and David Pollard. "Nucleation and growth of strike slip faults in granite." *Journal of Geophysical Research*. 88(B1): 555-568, 1983.
- Shewchuk, Jonathan Richard. *Triangle: Engineering a 2D Quality Mesh Generator and Delaunay Triangulator*. "Applied computational geometry: towards geometric engineering." Ming C. Lin and Dinesh Manocha, eds., volume 1148 of Lecture Notes in Computer Science. Berlin: Springer-Verlag, 1996.
- Srigutomo, Wahyu. "Gaver-Stehfest algorithm for inverse Laplace transform." Matlab Central: An open exchange for the MATLAB and Simulink user community. <<http://www.mathworks.com/matlabcentral/fileexchange/9987>>. Uploaded 15 Feb 2006. Accessed 25 Aug 2009.
- Srivastava, R.M. "Field verification of a geostatistical method for simulating fracture network models." The 41st U.S. Symposium on Rock Mechanics (USRMS). Golden, Colorado, 2006.
- Strang, Gilbert. Linear Algebra and its Applications. 4th ed. Belmont, CA: Thomson Higher Learning, 2006.
- Swenson, D. and B. Hardeman. "The effects of thermal deformation on flow in a jointed geothermal reservoir." 36th Rock Mechanics Symposium, ISRM International Symposium, New York, NY, 1997.

- Tamagawa, T., T. Matsuura, T. Anraku, K. Tezuka, and T. Namikawa. "Construction of fracture network model using static and dynamic data." *SPE 77741*, 2002.
- Tamagawa, T. and D. Pollard. "Fracture permeability created by perturbed stress fields around active faults in a fractured basement reservoir." *AAPG Bulletin*. 92(6): 743-764, 2008.
- Tester, J. (ed). "The future of geothermal energy: impact of Enhanced Geothermal Systems (EGS) on the United States in the 21st Century." MIT Report, 2007.
- Tezuka, K. and H. Niitsuma. "Stress estimated using microseismic clusters and its relationship to the fracture system of the Hijori hot dry rock reservoir." *Engineering Geology*. 56: 47-62, 2000.
- Tischner, T., Pfender, M. and Teza, D.: "Hot dry rock projekt Soultz: erste phase der erstellungeiner wissenschaftlichen pilotanlage." Bundesministerium für Umwelt, Naturschutz und Reaktorsicherheit, 2006.
- Valley, Benoît and Keith Evans. "Stress state at Soultz-Sout-Forêts to 5 km depth from wellbore failure and hydraulic observations." *Proceedings, Thirty-Second Workshop on Geothermal Reservoir Engineering*, Stanford University, 2007.
- Vandamme, L. and J.H. Curran. "A three-dimensional hydraulic fracturing simulator." *International Journal for Numerical Methods in Engineering*. 28: 909-927, 1989.
- Vinsome, P.K.W. and J. Westerveld. "A simple method for predicting cap and base rock heat losses in thermal reservoir simulators." *Journal of Canadian Petroleum Technology*. 19(3): 87-90.
- Wiles, T. and J. Curran. "A general 3-D displacement discontinuity method." Proceedings of the Fourth International Conference on Numerical Methods in Geomechanics. Z. Eisenstein, ed. Edmonton, Canada. Rotterdam: A.A. Balkema, 1982, 103-111.
- Willis-Richards, J., K. Watanabe, and H. Takahashi. "Progress toward a stochastic rock mechanics model of engineered geothermal systems." *Journal of Geophysical Research*. 101(B8): 17,481-17,496, 1996.
- Wrobel, L.C. The Boundary Element Method. Vol. 1. West Sussex, England: John Wiley & Sons, Ltd., 2002.
- Wu, Haiqing. "Imaging 3-D fracture networks around boreholes." *AAPG Bulletin*. 86(4): 593-604, 2002.
- Yamamoto, T., K. Kitano, Y. Fujimitsu and H. Ohnishi. "Application of simulation code, GEOTH3D, on the Ogachi HDR site." *Proceedings, 22rd Annual Workshop on Geothermal Reservoir Engineering*, Stanford University, 1997.
- Yeo, I.W., M.H. DeFreitas, and R.W. Zimmerman. "Effect of shear displacement on the aperture and permeability of a rock fracture." *International Journal of Rock Mechanics*, 35: 1051-1070, 1998.

- Yoshioka, K., B. Izgec, and R. Pasikki. "Optimization of geothermal well stimulation design using a geomechanical reservoir simulator." *Proceedings, Thirty-Third Workshop on Geothermal Reservoir Engineering*. Stanford University, 2008.
- Young, S. "Geometry and mechanics of normal faults with emphasis on 3D seismic data, conjugate faults, and the effects of sedimentary layering." PhD Thesis, Stanford University, 2001.
- Zoback, Mark. Reservoir Geomechanics. New York: Cambridge University Press, 2007.

Appendix A

A. Einstein Notation

Einstein notation is used to simplify the equations. A subscript indicates that a vector is being represented:

$$x_i = \begin{bmatrix} x_1 \\ x_2 \\ x_3 \end{bmatrix} \quad (\text{A-1})$$

Repeating indices indicate summation over the three dimensions:

$$x_{ii} = x_{11} + x_{22} + x_{33} \quad (\text{A-2})$$

Two different indices indicates a matrix:

$$x_{ij} = \begin{bmatrix} x_{11} & x_{12} & x_{13} \\ x_{21} & x_{22} & x_{23} \\ x_{31} & x_{32} & x_{33} \end{bmatrix} \quad (\text{A-3})$$

A partial derivative is indicated with a comma:

$$f_{,i} = \begin{bmatrix} \frac{\partial f}{\partial x_1} \\ \frac{\partial f}{\partial x_2} \\ \frac{\partial f}{\partial x_3} \end{bmatrix} \quad (\text{A-4})$$

The Laplacian can be written:

$$\nabla^2 f = f_{,ii} = \frac{\partial^2 f}{\partial x_1^2} + \frac{\partial^2 f}{\partial x_2^2} + \frac{\partial^2 f}{\partial x_3^2} \quad (\text{A-5})$$

The Kronecker delta is used in this report. It is defined as

$$\delta_{ij} = 1 \tag{A-6}$$

if $i = j$

$$\delta_{ij} = 0$$

if $i \neq j$